

# Concerting magnesium implant degradation facilitates local chemotherapy in tumor-associated bone defect

Qingqing Guan<sup>a</sup>, Tu Hu<sup>b</sup>, Lei Zhang<sup>a</sup>, Mengjiao Yu<sup>a</sup>, Jialin Niu<sup>a</sup>, Zhiguang Ding<sup>a</sup>, Pei Yu<sup>c</sup>, Guangyin Yuan<sup>a</sup>, Zhiquan An<sup>b, \*\*</sup>, Jia Pei<sup>a, d, \*</sup>

<sup>a</sup> National Engineering Research Center of Light Alloy Net Forming, Center of Hydrogen Science & State Key Laboratory of Metal Matrix Composite, School of Materials Science and Engineering, Shanghai Jiao Tong University, Shanghai, 200240, China

<sup>b</sup> Department of Orthopedics, Shanghai Jiao Tong University Affiliated Sixth People's Hospital, Shanghai Jiao Tong University, Shanghai, 200233, China

<sup>c</sup> Department of Orthopedics, Ruijin Hospital Affiliated to Shanghai Jiao Tong University School of Medicine, Shanghai Jiao Tong University, Shanghai, 200025, China

<sup>d</sup> Institute of Medical Robotics & National Engineering Research Center for Advanced Magnetic Resonance Technologies for Diagnosis and Therapy, Shanghai Jiao Tong University, Shanghai, 200240, China

## ARTICLE INFO

### Keywords:

Tumor-associated bone defect  
Biodegradable magnesium-based implant  
Multifunctional composite coating  
Bone regeneration  
Local tumor therapy

## ABSTRACT

Effective management of malignant tumor-induced bone defects remains challenging due to severe systemic side effects, substantial tumor recurrence, and long-lasting bone reconstruction post tumor resection. Magnesium and its alloys have recently emerged in clinics as orthopedics implantable metals but mostly restricted to mechanical devices. Here, by deposition of calcium-based bilayer coating on the surface, a Mg-based composite implant platform is developed with tailored degradation characteristics, simultaneously integrated with chemotherapeutic (Taxol) loading capacity. The delicate modulation of Mg degradation occurring in aqueous environment is observed to play dual roles, not only in eliciting desirable osteoinductivity, but allows for modification of tumor microenvironment (TME) owing to the continuous release of degradation products. Specifically, the sustainable H<sub>2</sub> evolution and Ca<sup>2+</sup> from the implant is distinguished to cooperate with local Taxol delivery to achieve superior antineoplastic activity through activating Cyt-c pathway to induce mitochondrial dysfunction, which in turn leads to significant tumor-growth inhibition *in vivo*. In addition, the local chemotherapeutic delivery of the implant minimizes toxicity and side effects, but markedly fosters osteogenesis and bone repair with appropriate structure degradation in rat femoral defect model. Taken together, a promising intrasosseous administration strategy with biodegradable Mg-based implants to facilitate tumor-associated bone defect is proposed.

## 1. Introduction

Bone cancers, which consists of primary and metastatic tumors, are the most severe and incurable bone disease globally, and have a deleterious influence on survival, quality of life and health expenditure [1–3]. Primary bone cancers, such as osteosarcoma and Ewing's sarcoma, always start in the bone or cartilage and are frequently diagnosed in children and adolescents [4]. In particular, osteosarcoma has become the second leading cause of tumor-related death in young people.

Metastatic bone cancers occur in 65–80 % of patients with breast and prostate cancers and are frequently found in lung, liver and kidney cancers [5–7]. At present, surgical intervention, consisting of resection of the bone-localized tumor followed by combined treatment of the surrounding tissues with chemo/radiotherapy, is the mainstream clinical modality for bone cancer to prevent recurrence, but has reached its limit of efficacy [8]. Moreover, traditional chemo/radiotherapy are often associated with inevitable problems including severe side effects of drugs to healthy tissues or even systemic toxicity, the development of

Peer review under responsibility of KeAi Communications Co., Ltd.

\* Corresponding author. National Engineering Research Center of Light Alloy Net Forming, Center of Hydrogen Science & State Key Laboratory of Metal Matrix Composite, School of Materials Science and Engineering, Shanghai Jiao Tong University, Shanghai, 200240, China.

\*\* Corresponding author.

E-mail addresses: [guanqq1009@sjtu.edu.cn](mailto:guanqq1009@sjtu.edu.cn) (Q. Guan), [zzuhutu@163.com](mailto:zzuhutu@163.com) (T. Hu), [lzhang880213@163.com](mailto:lzhang880213@163.com) (L. Zhang), [ymj454426356@126.com](mailto:ymj454426356@126.com) (M. Yu), [niujialin@sjtu.edu.cn](mailto:niujialin@sjtu.edu.cn) (J. Niu), [Dston1@gmail.com](mailto:Dston1@gmail.com) (Z. Ding), [yupei\\_ortho@163.com](mailto:yupei_ortho@163.com) (P. Yu), [gyyuan@sjtu.edu.cn](mailto:gyyuan@sjtu.edu.cn) (G. Yuan), [anzhiqian@126.com](mailto:anzhiqian@126.com) (Z. An), [jpei@sjtu.edu.cn](mailto:jpei@sjtu.edu.cn) (J. Pei).

<https://doi.org/10.1016/j.bioactmat.2024.06.026>

Received 24 April 2024; Received in revised form 18 June 2024; Accepted 18 June 2024

2452-199X/© 2024 The Authors. Publishing services by Elsevier B.V. on behalf of KeAi Communications Co. Ltd. This is an open access article under the CC BY-NC-ND license (<http://creativecommons.org/licenses/by-nc-nd/4.0/>).

resistance, and inadequate bioeffects on the defected bone tissues [9–11]. It thus motivates efforts to develop innovative therapeutic options with compelling biosafety and efficacy, among which local bone therapy [12–14] through the employment of a drug carrier or implant biomaterial to diseased bone tissue has recently emerged as an attractive strategy [15].

Surgical intervention of tumor-associated bone defect often leads to difficult to treat bone defects [16]. In addition to clinical autograft and allograft transplant, bone substitute biomaterials with favorable osteogenesis capability provide another promising avenue for facilitating the healing of bone defects after tumor resection. Furthermore, to reduce the risk of local bone cancer recurrence, it is essential to eliminate residual tumor cells around bone defects [17]. Suitable biomaterials capable of simultaneously providing anti-tumor therapy and promoting bone regeneration are thus favored, whereas many implant materials often suffer from one or more drawbacks, e.g. poor bioactivity, lack sufficient mechanical strength, etc. Resulting in unsatisfactory *in vivo* outcomes [18]. Magnesium (Mg) and its alloys have recently been proposed as a new-generation biodegradable implant material in the orthopedic field. In contrast to permanent biometals, Mg eliminates the need for a second surgical intervention to remove the implant and minimize stress shielding effects because of their similar elastic modulus to that of natural bones [19]. Moreover, recent studies have revealed the desirable, stimulatory effects of its main degradation products of  $Mg^{2+}$  on directed osteogenic differentiation and facilitating fracture repair [20], thus revealing its great therapeutic potential in treating bone diseased. Nevertheless, detrimental effects of overfast degradation of Mg implant have also been observed, including the gas cavity formed by burst hydrogen ( $H_2$ ) release of Mg implant, and moreover, deterioration of biocompatibility and the complexity of the  $Mg^{2+}$ -induced immunomodulation on macrophages and bone resorption [21], which hamper bone regeneration, thus emphasizing the importance of degradation control. To effectively satisfy the genuine demands of orthopedic implants, it is imperative to corrosion rate while maintain mechanical integrity for an extended duration, and to limit the emission of  $H_2$ , which can be accomplished through the process of alloying or other preparatory techniques [22,23]. A complementary approach to advancing the technology of Mg alloys is through surface modification. The utilization of coatings is a viable strategy to bolster the resistance to corrosion and the biocompatibility of the implants. On the other hand, it has been reported that the high alkalinity and  $H_2$  gas generated during the degradation of naked Mg have cytotoxic effects on osteosarcoma cells *in vitro* [24]. However, achieving significant and long-term  $H_2$  release in the tumor to produce the best anticancer therapeutic impact is still

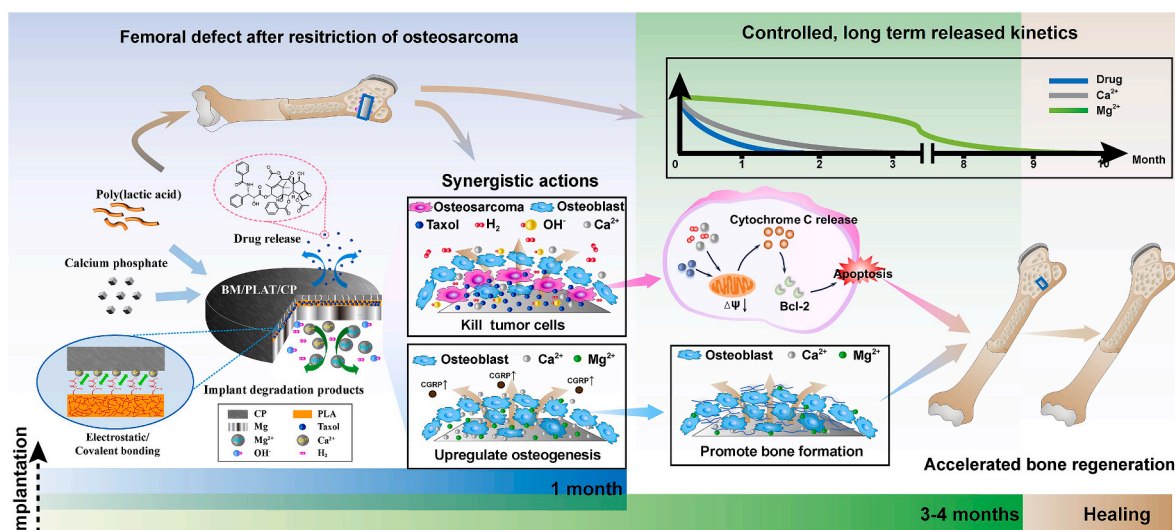
problematic [25,26]. Therefore, in addition to alloying and processing the Mg matrix, it is important and necessary to regulate the Mg biodegradation through the development of a rational design surface coating for appropriately exerting its beneficial role in facilitating bone reconstruction and repair while combating bone tumor recurrence [27, 28].

Apart from magnesium, calcium and lots of its compounds are well-advocated to promote osteoblast proliferation, migration and osteogenic differentiation. Furthermore, calcium ions ( $Ca^{2+}$ ) can also play a vital role in tumor therapy through activating mitochondrial apoptosis pathways, resulting in  $Ca^{2+}$ -overloading-induced cancer cell death [29, 30]. Hence, to integrate the multifunctionalities required for treating tumor-induced bone defect, herein, we propose the development of a Mg-based composite implant (BM/PLAT/CP) through fabrication of a bilayer coating platform with chemotherapeutic loading capacity, and tailored degradation characteristics for synergistic local therapy (Scheme 1). The bilayer coating consists of an inner layer of poly (lactic acid) with typical chemotherapy drug-Taxol (abbreviated as PLAT) and an outer layer of calcium phosphate-based rough coating (CP). The resultant implant is capable of locally co-delivering Mg biodegradation products and chemotherapeutic drugs in a well-controlled, sustained manner. Taking the advantages, we postulate that this Mg-based implant could concurrently promote the formation of new bones and alleviate or even prevent bone tumor recurrence and consequently offer superior efficacy in treating tumor-induced bone defects, owing to the appropriate control of the overfast Mg degradation and the sustainable release of degradation products ( $Ca^{2+}$ ,  $H_2$ ) to synergize the local chemotherapeutics. The *in vitro* viability, direct adhesion and proliferation of cells on the implant surface and the influence of the degradation extracts, are studied in combination with MC3T3 osteoblasts and MNNG osteosarcoma cells, respectively. The preliminary anti-tumor mechanism with this local implant strategy is also explored. The corresponding *in vivo* effects on tumor-induced bone defect are investigated in nude mice with osteosarcoma and in Sprague–Dawley (SD) rats with femoral defects, respectively.

## 2. Results

### 2.1. Mg-based implant characterization

The biodegradable BM/PLAT/CP implant was prepared and deposited with a bilayer coating platform of poly (lactic acid) (PLA)/calcium phosphate (CP). Fig. 1a confirmed that the composite implants consisted of designated coatings with an inner layer of PLA loaded with a typical



Scheme 1. Schematic diagram of BM/PLAT/CP implant design and bio-application in treating tumor-induced bone defects.

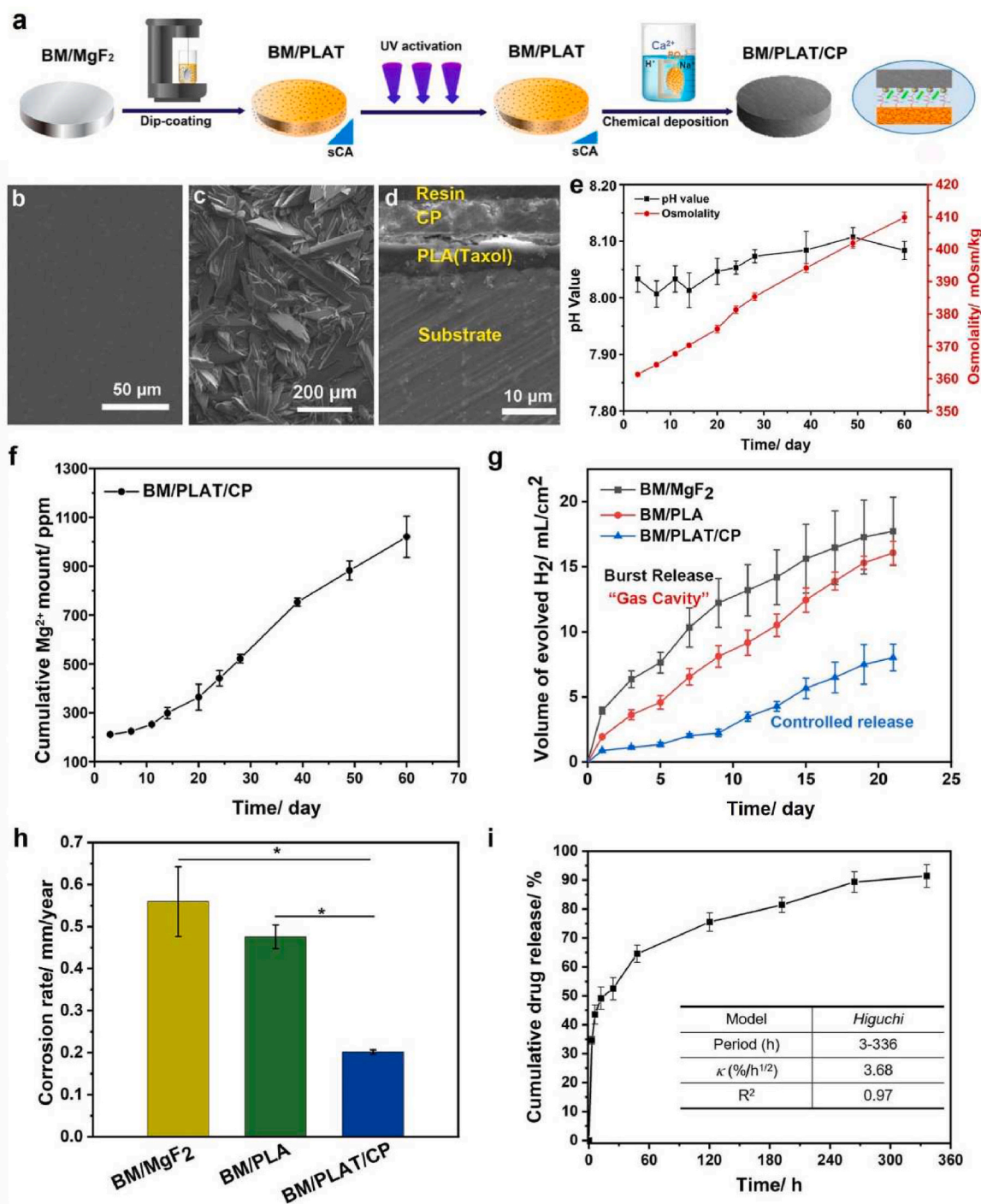


**Fig. 1.** Preparation and characterization of BM/PLAT/CP. **a**) The process of the bilayer coatings on Mg-implant. **b**) SEM image of the top view of BM/PLAT implants. **c**, **d**) SEM images of the top view and cross-section view of BM/PLAT/CP implants. **e**) pH and osmolality and **f**) cumulative Mg<sup>2+</sup> amount profiles of BM/PLAT/CP during 60 days of immersion in DMEM. **g**) *In vitro* H<sub>2</sub> release profile of BM-based implants in phosphate-buffered saline with 0.1 % Tween 20 (PBST) for 21 days. **h**) Calculated *in vitro* corrosion rate of BM/MgF<sub>2</sub>, BM/PLA and BM/PLAT/CP. **i**) *In vitro* Taxol release profile of BM/PLAT/CP implants in PBST for 2 weeks. \*p < 0.05.

chemotherapeutic Taxol, and an outer layer of CP, aiming to simultaneously regulate the biocorrosion, improve biocompatibility and osteogenesis of the Mg-based substrate, integrated with synergistic antineoplastic activity. The thicknesses of the bilayer coatings were optimized for this study to obtain a suitable implant degradation profile to match new bone growth, meanwhile maintaining a sustainable, controlled release of both drugs and degradation products for desirable bio-efficacy. Additionally, the morphology of the outermost layer was also modulated and optimized through chemical solution synthesis to

achieve favorable osteoblastic cell responses [31]. In Fig. 1b it clearly exhibited that the as-prepared PLAT coating was intact and uniform, and importantly, there was no obvious drug aggregates or microphase separation. Cross-sectional SEM images of the BM/PLAT/CP implant were shown in Fig. 1c and d. Fig. 1c illustrated the presence of numerous degraded CP flakes on the surface of the BM/PLAT/CP specimens. The CP layer, characterized by water lily structure, exhibited approximately 200 μm in length and several tens of micrometers in width and thickness on account of the heterogeneous nucleation of calcium phosphate on the

UV-pretreated PLA film. The microscale-rough CP layer with a nested structure completely covered the PLA coating loaded with Taxol. The thicknesses of the PLA layers loaded with Taxol and the outermost brushite layer were determined of  $\sim 3 \mu\text{m}$  and  $\sim 6\text{--}7 \mu\text{m}$ , respectively (Fig. 1d). As shown in Fig. S1, the surface roughness of BM/PLAT/CP was determined to be  $4.15 \pm 0.3 \mu\text{m}$  using a stylus surface profiler. This surface microroughness might contribute to the promoted adhesion and proliferation of osteoblastic cells, as compared to the smoother surfaces including BM/MgF<sub>2</sub> ( $0.31 \pm 0.13 \mu\text{m}$ ) and BM/PLA ( $0.21 \pm 0.10 \mu\text{m}$ ), according to several previous reports on the effects of microroughness on osteoblasts [32]. In addition, the adhesion of the composite coating was evaluated using the “Tape Test”, as illustrated in the representative image shown in Fig. S2. The test revealed that the surface remained intact which corresponds to an ASTM 5B rating, indicating excellent adhesion with less than 5 % of the coating being removed or detached. These findings confirmed that the bilayer coatings could adhere tightly to each other and to the underlying Mg-based substrate. The excellent adhesion was most likely due to the strong coordination interaction between the abundant carboxylic ester groups of PLA and the Ca<sup>2+</sup> in CP coatings.

## 2.2. *In vitro* degradation and drug release

The *in vitro* degradation product release profiles and calculated degradation rates of BM/PLAT/CP implants for up to 2 months were displayed in Fig. 1e–h. In contrast to the previously reported naked Mg alloy, the pH of the BM/PLAT/CP group during degradation only increased gently to  $\sim 8.10$  of desirable weak alkalinity, and the osmolality and cumulative release profile of Mg<sup>2+</sup> exhibited a nearly linear growth trend, which were considerably reduced. H<sub>2</sub> evolution during Mg degradation was carefully monitored, which also served as a quantitative indicator of the *in vitro* magnesium corrosion rate. Fig. 1g clearly revealed that BM/MgF<sub>2</sub> generated a burst release, particularly for the first 3 days, and it only slightly decreased with BM/PLA, which could result in unfavorable gas cavity upon implantation. On the contrary, BM/PLAT/CP showed well-controlled, more sustainable hydrogen evolution, and the accumulative amount was only about half of that produced from BM/PLA. In the extract, the Ca<sup>2+</sup> concentration of DMEM medium gradually decreased from 91.0 ppm to around 30.0–40.0 ppm, which indicated slow-release manner of Ca<sup>2+</sup> (Fig. S3). Moreover, the concentration of Mg<sup>2+</sup> ions in the extraction solution gradually decreased as the coating thickness increases due to the additional CP coating was engineered to enhance corrosion resistance as a physical barrier, suggesting a retarded degradation provided by the bilayer coating, in contrast to the bare substrate, and PLA coating alone (Fig. S4). According to ASTM G31-72, the calculated *in vitro* corrosion rate of BM/PLAT/CP ( $0.201 \pm 0.005 \text{ mm/year}$ ) groups was markedly modulated and significantly lower than those of the BM/MgF<sub>2</sub> and BM/PLA groups. Notably, there was little interference in terms of degradation with the incorporation of the Taxol drug into the composite coating (Fig. 1h).

The *in vitro* kinetic release profile of chemotherapeutic Taxol from the BM/PLAT/CP implant over 2 weeks was plotted in Fig. 1i. The amount of Taxol released from the BM/PLAT/CP implant was approximately 52.5 % post 3 days and 91.0 % for the two weeks, in accordance with a diffusion-controlled drug release mechanism by using a Higuchi model analysis [33]. It was noteworthy that the compact CP top layer dramatically alleviated the overfast release of Taxol in the early stage and subsequently regulated drug release kinetics [34]. These results demonstrated that the BM/PLAT/CP implant showed promise in acting as a local drug delivery system for long-term use.

## 2.3. *In vitro* effect of the BM/PLAT/CP implant on osteosarcoma and osteoblastic cells

### 2.3.1. *In vitro* biocompatibility and bioactivity on osteoblastic cells

To evaluate the *in vitro* biocompatibility and osteoconductivity of the composite implant, a direct osteoblastic cell adhesion assay was first performed on different samples. As shown in Fig. 2a and b, slightly enhanced initial MC3T3-E1 cell adhesion was observed after 1 day of incubation in both the BM/CP and BM/PLAT/CP groups compared to that in control group ( $p < 0.05$ ). On Day 3 and Day 5, the two groups showed adherent cell density comparable to that of the control group, although in the BM/PLAT/CP group it was slightly lower than that in the BM/CP without Taxol loading, revealing negligible influence of this Taxol-loaded coating on exacerbating osteoblast biocompatibility. In contrast, the adherent live cells in the BM/MgF<sub>2</sub> group were significantly reduced, which exhibited a shrunk, roundish or abnormal morphology, demonstrating acute cytotoxicity resulting from initial adhesion and subsequent cell growth. This difference may be predominantly attributed to the rapid degradation of the Mg matrix, which lacked effective protection from the outermost brushite coating, thus inducing excessive Mg<sup>2+</sup>, osmolality and possibly overhigh alkaline environment. The viabilities of MC3T3-E1 cells incubated with extracts of BM/MgF<sub>2</sub>, BM/CP and BM/PLAT/CP for 1, 3 and 5 days were displayed in Fig. 2c. After culturing for 3 days, the BM/MgF<sub>2</sub> group clearly presented distinct toxicity to MC3T3-E1 cells, revealing poor viability of  $\sim 56 \%$ . Both the BM/CP and BM/PLAT/CP groups exhibited good cytocompatibility for MC3T3-E1 osteoblastic cells, achieving favorable viability of  $\sim 113 \%$  and  $\sim 91 \%$  on Day 5, respectively, thus meeting the biocompatibility requirements of ISO10993-5 for clinical use.

To assess potential osteoinductivity *in vitro*, after 7 and 14 days of culture in differentiation medium, analysis of ALP activity demonstrated that early osteogenic activity was strongly boosted in the BM/CP and BM/PLAT/CP groups, and there was no significant difference between these two groups (Fig. 2d). Real-time PCR results after 14 days of culture were shown in Fig. 2e. Similarly, compared with those in the Ti control group, Alp and Opn expressions in the BM/CP and BM/PLAT/CP groups considerably elevated, and the Col I expression was also slightly greater in the BM/PLAT/CP group. Runx 2 expression was significantly upregulated in the BM/CP group, which was slightly higher compared to BM/PLAT/CP groups. These features indicated the prominent *in vitro* osteogenic potential of Mg-based implants achieved via this rational-designed bilayer coating system, with negligible influence of drug loading observed on osteoblast biocompatibility.

### 2.3.2. *In vitro* cytotoxic effect on osteosarcoma cells

To explore the *in vitro* inhibitory effects of the Mg-based implants on osteosarcoma cells, direct cell adhesion and cell viability assays were performed with MNNG cell line. The cell adhesion density, morphology and viability after 1, 3, and 5 days of culture are displayed in Fig. 3. During the entire culture period, compared with the control group, the adherent live cell density in the BM/PLAT/CP groups was significantly lessened, with cell morphology in the abnormal state, which was further minimized to almost 0 on Day 5, indicating a superior suppressive effect of BM/PLAT/CP on osteosarcoma cells (Fig. 3a and b). As for the BM/MgF<sub>2</sub> group, the osteosarcoma cell density gradually decreased to 5.48 (cell/mm<sup>2</sup>) and was also much lower than that in the control group on Day 5, which was most probably attributed to the high osmolality, alkaline environment and burst H<sub>2</sub> release associated with overfast Mg biodegradation. Interestingly, for the BM/CP group, a reduced initial tumor cell adhesion was observed after 1 day of incubation, suggesting distinct inhibition on osteosarcoma cell proliferation directly on the BM/CP surfaces.

To determine the possible effect of the released degradation products on modulating tumor microenvironment (TME), the viability of MNNG cells incubated with extracts of different BM-based samples was detected (Fig. 3c). Throughout the entire assay, the extracts of the BM/MgF<sub>2</sub>, BM/

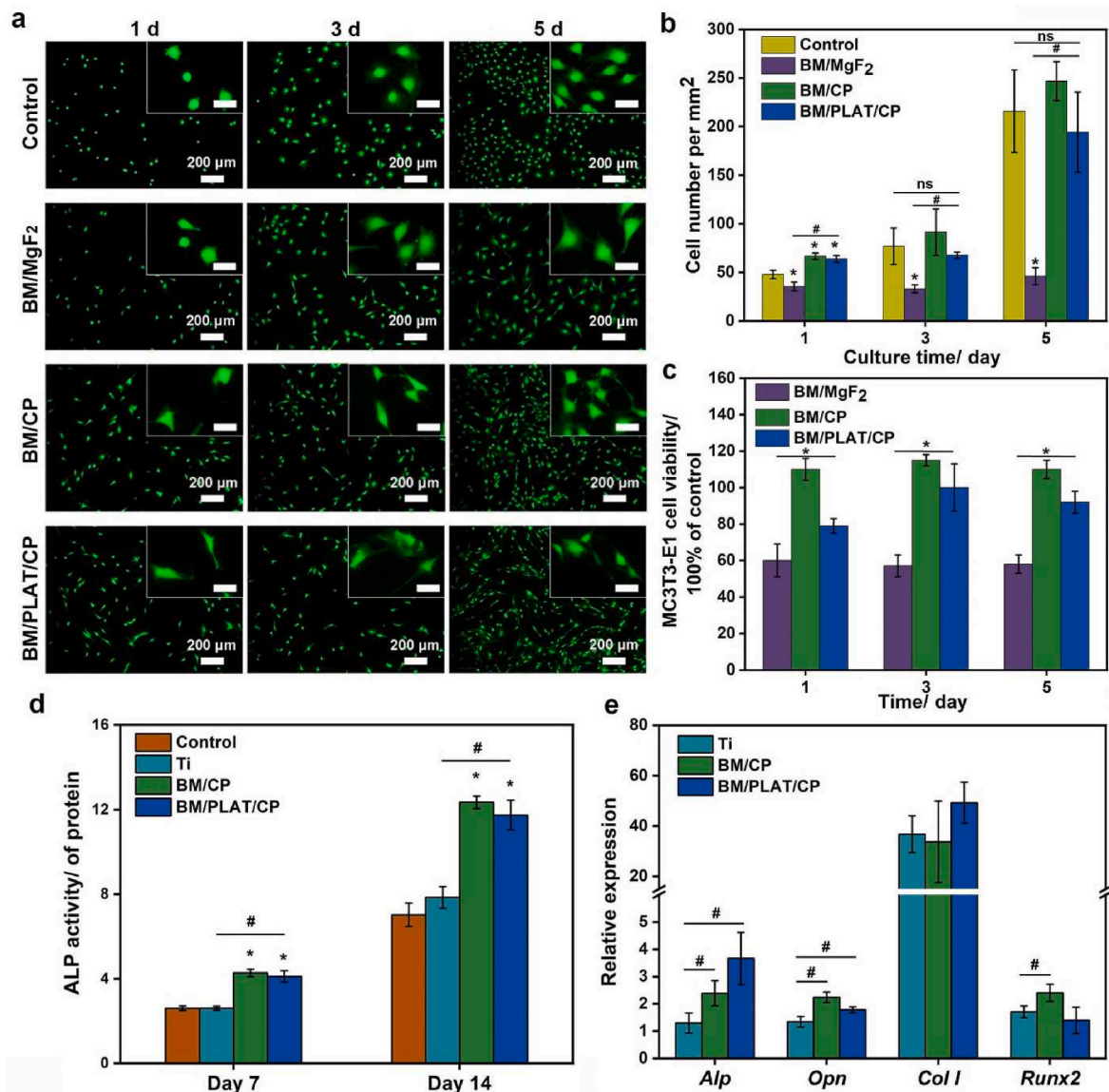


**Fig. 2.** *In vitro* effect of different implant extract on MC3T3-E1 cell response. a) Fluorescent microscopy images and b) adherent cell density of MC3T3-E1 osteoblastic cells incubated with different implants. Scale bar = 200 and 100  $\mu\text{m}$ , respectively. c) Cell viability and d) ALP activities of MC3T3-E1 cells cultured in samples extracts. e) RT-PCR results of expression of osteogenic genes *Alp*, *Opn*, *Col 1* and *Runx 2* after 14 days of culture. <sup>ns</sup> $p > 0.05$  vs. Control group, <sup>\*</sup> $p < 0.05$  vs. Control group; <sup>#</sup> $p < 0.05$ .

CP and BM/PLAT/CP groups all exhibited significant inhibitory effects on osteosarcoma cells and their proliferation. It should be noteworthy that the antineoplastic effect of the extracts was not as significant as those directly attached to the sample surface, and it thus may be mostly attributed to the local  $\text{H}_2$  evolution directly from the Mg-based samples, which was absent in the sample extracts.

### 2.3.3. *In vitro* effect of Mg degradation microenvironment on differentiating osteoblast vs. osteosarcoma cells

Considering the high reaction activity of Mg in aqueous environments, to evaluate the effect of the degradation products of BM-based composite implants on differentiating viability of osteoblast and osteosarcoma cells was essential for rational design and appropriate control of Mg degradation. In this study, the Mg biodegradation products consisted mainly of gaseous  $\text{H}_2$ ,  $\text{Mg}^{2+}$  and  $\text{OH}^-$ , which could be characterized by the  $\text{Mg}^{2+}$  concentration, pH, and osmolality of the extract. To further explore these degradation factors that may affect the viability of bone cells, BM extracts were prepared with a series of dilutions (100 % BM,

80 % BM, 50 % BM, and 20 % BM). The viability of MNNG osteosarcoma cells and MC3T3-E1 osteoblasts cultured in the extracts for 1, 3 and 5 days was displayed in Fig. 4a and b. The 100 % BM and 80 % BM extracts exhibited evident cytotoxic effects on both osteosarcoma and osteoblastic cells, which could be due to the overhigh pH, osmolality and even  $\text{Mg}^{2+}$ . Apparently, the osteoblastic cells bear effect of extract better than osteosarcoma cells, which exhibited  $\sim 86\%$  of cell viability on day 5 in 80 % BM group. The conditions of 50 % BM exerted certain cytotoxic effect on osteosarcoma cells without inhibiting osteoblasts that the cell viability both exceeded 80 % on day 3 and 5. The 20 % BM extracts were approaching to the physiological conditions, thus showing limited inhibitory effect on osteosarcoma, but rather boosting osteoblast viability. Upon the incorporation of slight amount of Taxol, the viability of osteosarcoma cells cultured in BM/PLAT/CP extract decreased drastically, and meanwhile that of osteoblastic cells was still greater than 75 %, indicating the advantage of local Taxol delivery for BM-based composite implant in killing osteosarcoma cells meanwhile showing minimized side effect on osteoblasts. The physicochemical parameters of the

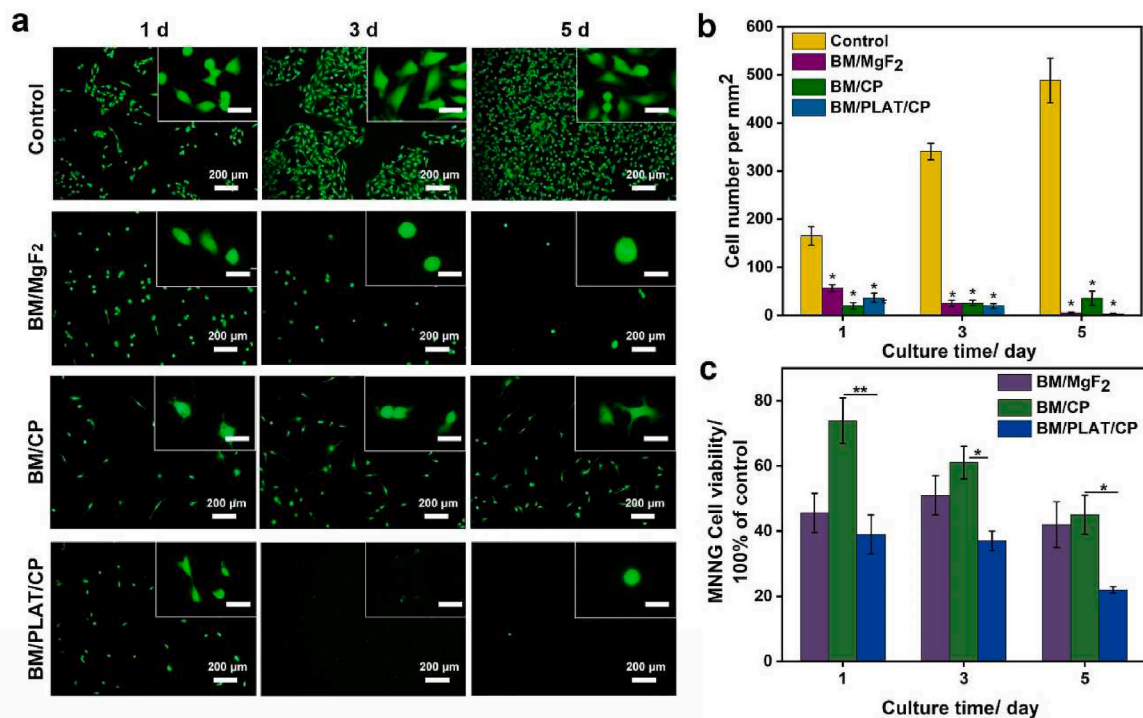


**Fig. 3.** *In vitro* killing effect on MNNG osteosarcoma cells. a) Fluorescent microscopy images and b) adherent cell density of MNNG osteosarcoma cells on control, BM/MgF<sub>2</sub>, BM/CP and BM/PLAT/CP samples, respectively. Inserted images in a) with higher magnification showed the cell spreading morphology, with scale bar represents 100 μm. c) Cell viability results of MNNG cells cultured with extract of BM/MgF<sub>2</sub>, BM/CP and BM/PLAT/CP, respectively. \**p* < 0.05, \*\**p* < 0.01.

extracts and the cell viability results of MNNG osteosarcoma cells cultured in these extracts are shown in Fig. 4c and d. The pH, osmolality, and Mg<sup>2+</sup> concentration of the BM extract gradually decreased with increasing dilution ratio. The BM/PLAT/CP extracts exhibited lower pH values, osmolalities, and Mg<sup>2+</sup> concentrations, whose values fell into those between the 20 % and 50 % BM extracts, suggesting a favorable modulation range of Mg degradation to exert cytotoxic effect on tumor cells whereas maintaining desirable osteoblast cytocompatibility (Fig. 4e).

#### 2.3.4. The mechanism of BM/PLAT/CP-induced osteosarcoma cytotoxicity

The complicated tumor microenvironment (TME) featured by acidic pH values, high levels of reactive oxygen species (ROS) and vascular abnormalities may greatly limit the effect of tumor therapy [35,36]. Recent studies had provided evidence supporting the potent anticancer capacity of gaseous H<sub>2</sub>, which may be attributed to the ability of a number of hydrogen molecules to entry into cells, thereby impairing the energy supply crucial for the survival of cancer cells [37]. Moreover, calcium ions (Ca<sup>2+</sup>) also exerted significant influence on various tumor cell processes. Notably, in the context of elevated Ca concentrations, calcium channels within cancer cells exhibited abnormal functionality, leading to an overload of calcium ions and subsequent mitochondrial damage. This calcium-induced impairment significantly contributed to the eradication of cancer cells [38]. To evaluate mitochondrial damage, we employed the commercially available dye JC-1 to detect changes in the mitochondrial membrane potential (MMP). The control group displayed weak green fluorescence, while the BM group showed greatly increased signals (Fig. 5a and b), indicating the H<sub>2</sub> released from BM greatly reduced MMP of tumors cells. The green fluorescence intensity further elevated in the BM/CP group, assumably due to the combined effect of H<sub>2</sub> and Ca<sup>2+</sup> stemmed from the composite Mg sample. Additionally, PTX was used to induce oxidative stress, resulting in mitochondrial damage. The BM/PLAT/CP group exhibited the most significant decrease in the MMP.

To further verify the uptake of Ca<sup>2+</sup> by tumor cells, we investigated

the intracellular Ca concentration using the Ca<sup>2+</sup> probe Fluo-4 AM. Fluorescence microscopy clearly revealed that, compared with the control group, both the BM/CP and BM/PLAT/CP groups exhibited enhanced green fluorescence, confirming the effect of overloaded Ca<sup>2+</sup>. Interestingly, the BM/CP group exhibited even 1.02-fold stronger intracellular signals than that of the BM/PLAT/CP group, which could be attributed to the release of PTX causing mitochondrial dysfunction and inhibiting intracellular Ca transport, as shown in Fig. 5c and d. The cytosol Ca<sup>2+</sup> accumulation would stimulate oxidase activity of cells that was responsible for ROS generation, and the process of Ca<sup>2+</sup>-associated ATP synthesis could also be restrained. Therefore, the intracellular ROS level was also detected and evaluated. Fig. 5e showed the elevated ROS level of MNNG tumor cells treated with BM/CP group. There was no statistical difference between BM/CP and control groups. After co-culturing for 24 h, it can be observed that BM/CP group induced nearly double intracellular ROS production compared to the control group (*p* < 0.05), which was most probably attributed to the accumulative Ca<sup>2+</sup> products. Furthermore, the intracellular ATP content in the BM-related group displayed a similar downward trend (Fig. 5f), and the BM/PLAT/CP group exhibited the greatest decrease by 31 % in the MMP and 80 % in intracellular ATP level compared to control group respectively, suggesting that the generated H<sub>2</sub> and Ca<sup>2+</sup> were capable of killing cancer cells via inhibiting mitochondrial function and ATP synthesis. This significant bioeffect can be attributed to the synergistic actions of Mg degradation products and local Taxol release by destroying the TME, which thus resulted in excessive toxicity to osteosarcoma cells. Additionally, Western Blot assays revealed significant upregulation of cytochrome C (Cyt-c) and downregulation of Bcl-2 in cells co-incubated with BM/PLAT/CP (Fig. 5g), which suggested the occurrence of multilevel mitochondrial damage, further confirming the dual therapeutic effects of calcium overloading and H<sub>2</sub> release, ultimately leading to increased levels of tumor cell apoptosis (Fig. 5h).

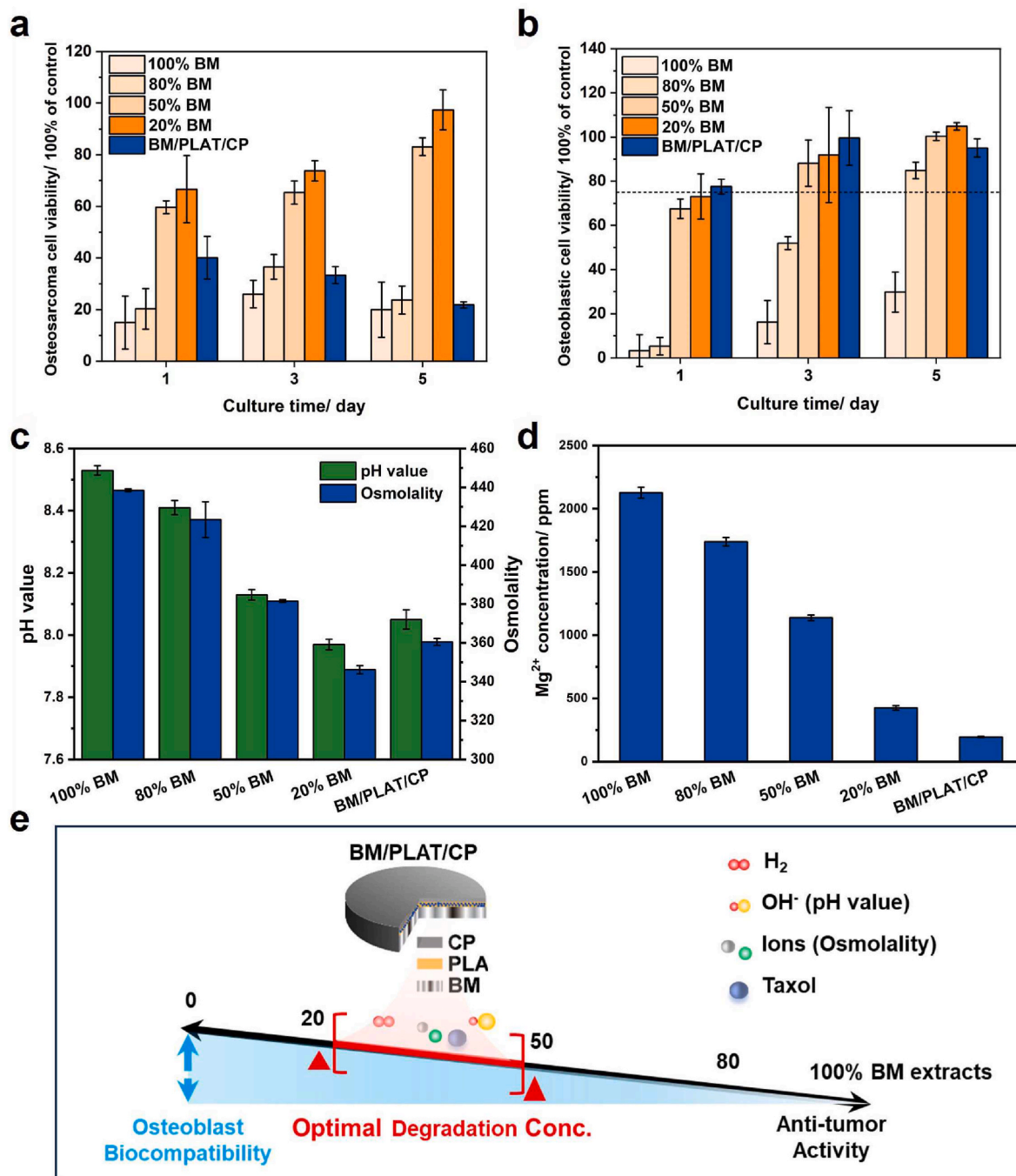


**Fig. 4.** Viability results of a) MNNG cells vs. b) MC3T3-E1 cells cultured in the BM extracts with dilutions and BM/PLAT/CP extract. c, d) pH value, osmolality and Mg<sup>2+</sup> concentration of BM extracts with dilutions (100 % BM, 80 % BM, 50 % BM and 20 % BM) and BM/PLAT/CP extract. e) Schematic illustration on the effect of degradation extracts of BM/PLAT/CP on differentiating viability between bone tissue cell and tumor cell.

**2.4. In vivo effect of the BM/PLAT/CP implant on localized bone tumor therapy**

To assess *in vivo* antitumor efficacy, BM/CP, BM/PLAT45/CP, and BM/PLAT150/CP samples were implanted into the site adjacent to the induced osteosarcoma of BALB/c nude mice (Fig. 6a). Saline and Taxol were injected as the negative and positive controls, respectively. Photographs of the tumors in the nude mice and changes in tumor volume at predetermined time intervals were presented in Fig. 6b–d. During the 7-day observation, as the tumor growth was barely affected in the negative control group, the largest tumor volume and the highest tumor growth rate were observed. Compared to the negative control group, the relative

tumor growth rates in the free Taxol injection, BM/CP, BM/PLAT45/CP, and BM/PLAT150/CP groups decreased by 23.3 %, 15.5 %, 31.3 % and 66.8 %, respectively. BM/CP, free Taxol injection and BM/PLAT45/CP all suppressed tumor growth, which was more prominent after 5 days. Among all the groups, the BM/PLAT150/CP had the greatest inhibitory effect on tumor growth during the entire period, and the difference in tumor volume was not significant even after 7 days. Notably, even without Taxol loading, tumor growth was still inhibited in the BM/CP group, although to a slight extent, whose effect was actually similar to that of the free Taxol injection group. This result therefore implied the suppressive role of accumulative Mg biodegradation products and calcium overloading. With the incorporation of local Taxol delivery, BM-

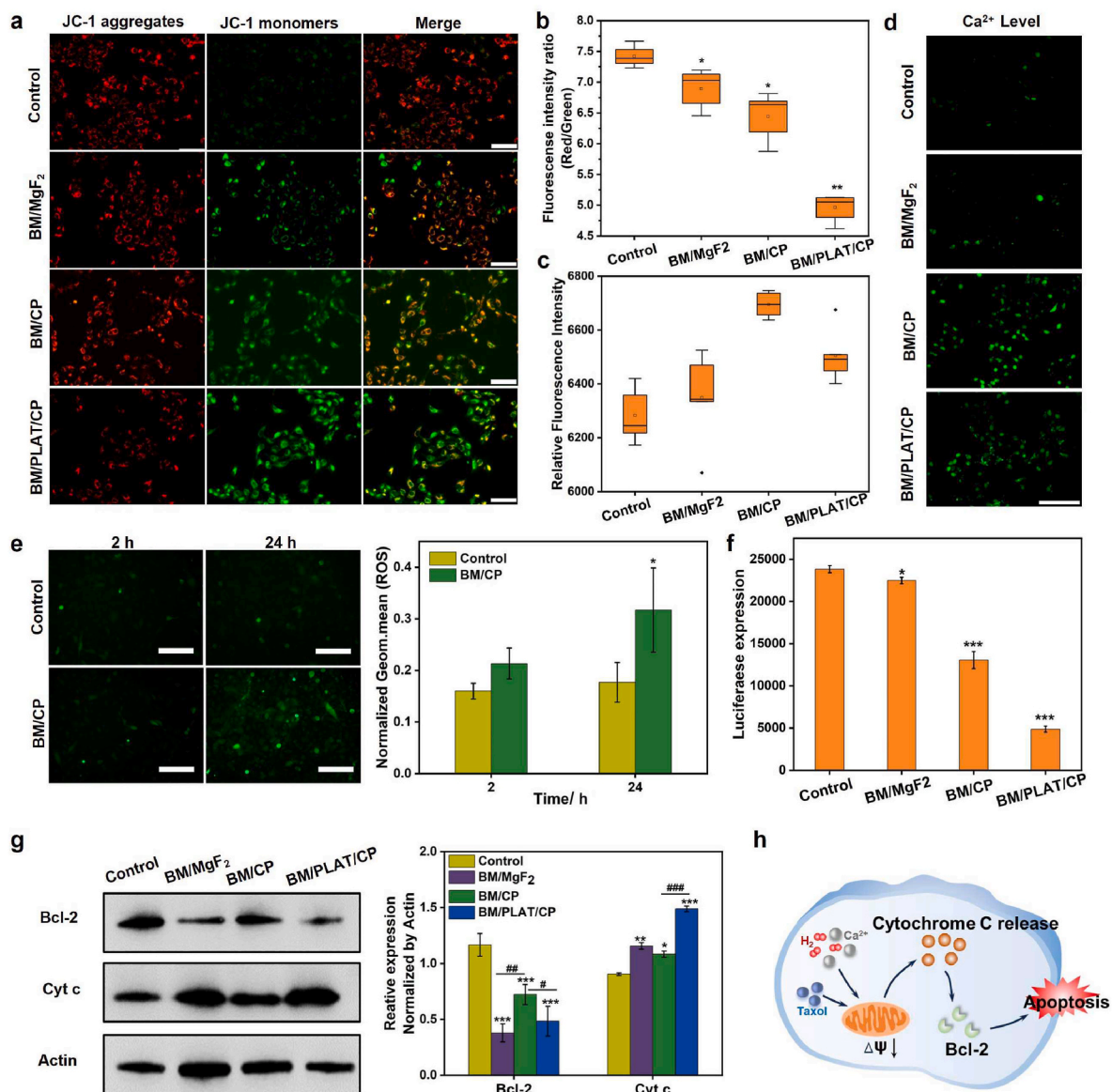


**Fig. 5.** The mechanism evaluations of BM/PLAT/CP implant induced osteosarcoma cytotoxicity. a, b) MMP of MNNG cells were treated with different samples. Scale bar: 50  $\mu\text{m}$ . c, d) Fluorescence microscope images and the corresponding ratio analysis of Ca<sup>2+</sup> ions released from different samples in MNNG cells. Scale bar: 100  $\mu\text{m}$ . e) ROS level of MNNG cells treating with BM/CP extract. Scale bar: 100  $\mu\text{m}$ . f) Intracellular ATP content analysis with different treatments (n = 3). g) Western blotting analysis of Cyt-c, and Bcl-2 proteins. h) Schematic diagram of proposed mechanism of BM/PLAT/CP. \*p < 0.05, \*\*p < 0.01, \*\*\*p < 0.001 vs. Control group. #p < 0.05, ##p < 0.01, ###p < 0.001.

based composite implants could maintain considerable tumor inhibition efficacy owing to the co-existence of sustained Taxol release. In addition, the tumor inhibition efficiency of BM/PLAT150/CP group was superior to that of conventional chemotherapy in the Taxol administration, indicating the advantage of local Taxol delivery, as well as the indispensable role of microenvironment modulation induced by controlled Mg degradation.

At the end of the experiment, tumor tissues were collected and evaluated via hematoxylin & eosin (H&E) staining. Fig. 6e showed representative tissue sections from the negative control, BM/CP, Taxol injection, and BM/PLAT150/CP groups. No visible damage to the tumor tissue was observed in the negative control group. The BM/CP and Taxol injection groups both revealed slight changes, and the BM/PLAT150/CP local treatment led to the most noticeable decrease in tumor cell numbers and changes in cell morphology, in which massive cell nuclei were dissolved and cell contact was loosened. The results of the quantitative analysis indicated that the tumor tissue necrosis rate reached

11.2  $\pm$  6.3 %, 39.4  $\pm$  6.0 %, and 67.4  $\pm$  5.2 % for the BM/CP, Taxol injection, and BM/PLAT150/CP implant groups, respectively (Fig. 6f). It can be clearly concluded that the tumor tissue necrosis rate followed the order of Control < Taxol injection  $\ll$  BM/PLAT150/CP. The BM-based composite implant demonstrated synergistic antitumor effects on osteosarcoma tumor-bearing mice, which was generally in accordance with the *in vitro* response of MNNG osteosarcoma cells (Fig. 3).

## 2.5. *In vivo* effect of the BM/PLAT/CP implant on femoral defect healing

### 2.5.1. *In vivo* evaluation of implant degradation

The *in vivo* osteogenic efficacy of BM/PLAT/CP was investigated after implanting into femoral defect model SD mice (Fig. 7a). Fig. 7b showed 3D-reconstructed micro-CT images of different implants at each time point. Throughout the entire *in vivo* experiment, the BM/CP and BM/PLAT/CP implants maintained structural integrity without disintegration. A statistical analysis of the residual volume, as shown in Fig. 7c

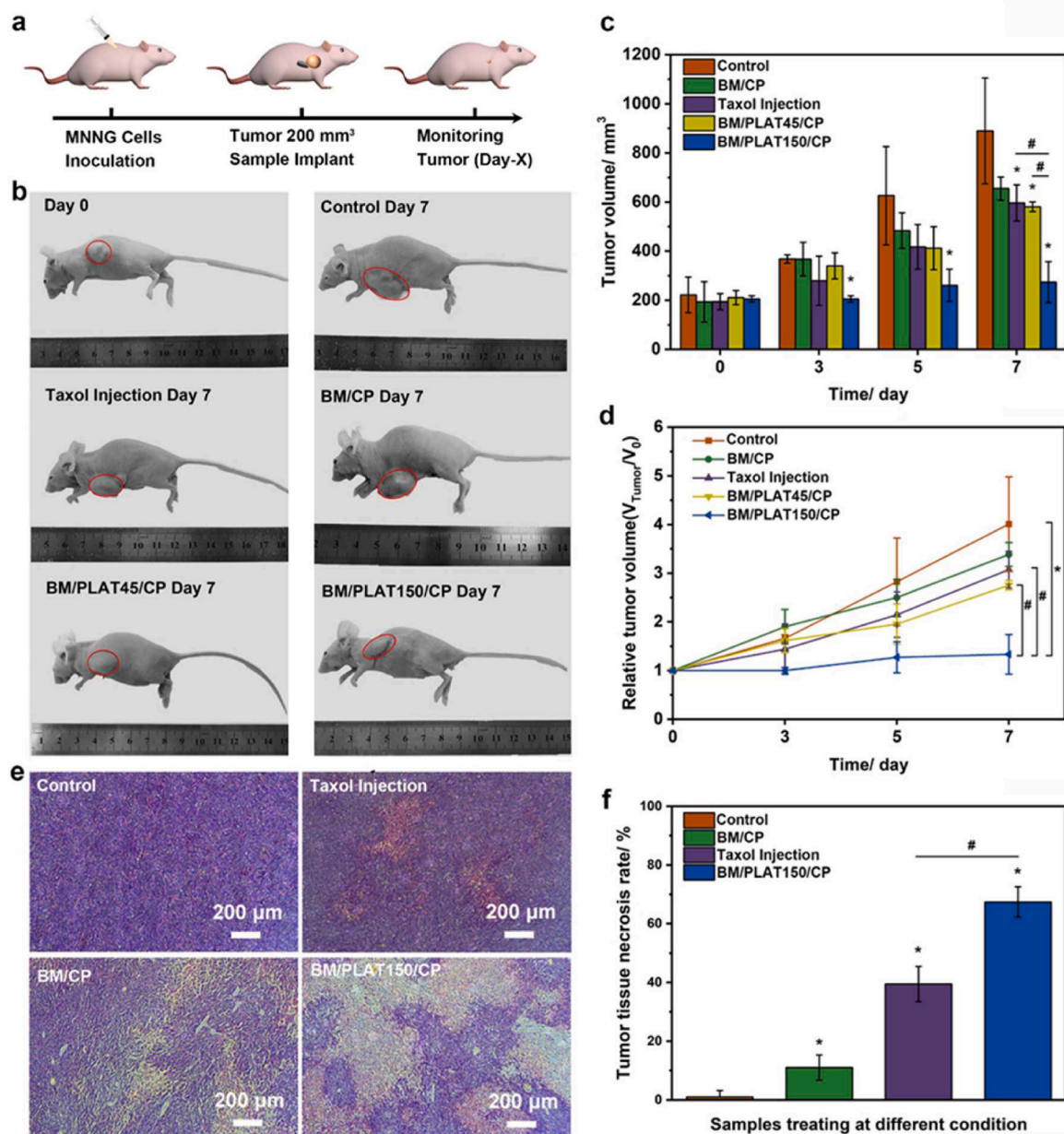


**Fig. 6.** The anti-tumor effect of BM-based implant on osteosarcoma tumor-bearing mice. a) Schematic illustration of MNNG-bearing mice and therapeutic process of implants. b) Tumor photographs of nude mice for the control, Taxol, BM/CP, Mg/PLAT45/CP, and Mg/PLAT150/CP groups at Day 0 and Day 7. c) Tumor volume and d) relative tumor volume change of five groups at each time point. e, f) H&E stained images of tumor tissue and tumor tissue necrosis rate for the control, Taxol, BM/CP, and Mg/PLAT150/CP groups. \* $p < 0.05$  vs. Control group. # $p < 0.05$ .

and d revealed that both BM-based implants gradually degraded *in vivo* in a well-controlled manner. The volume reduction in the BM/PLAT/CP group was slightly greater than that in the BM/CP group, about 9.56%. This difference was presumably due to the micro-defect in the PLA coating after Taxol release, which slightly undermined the corrosion protection of the Mg implant. According to the volume loss, the *in vivo* degradation rate of the BM/PLAT/CP implant was determined of  $0.46 \pm 0.03$  mm/year during the initial 8 weeks post-implantation. Subsequently, the degradation rate slightly increased to  $0.47 \pm 0.08$  mm/year and  $0.66 \pm 0.10$  mm/year at 12 and 16 weeks post-surgery, respectively, which could sufficiently meet clinical requirements.

### 2.5.2. Micro-CT evaluation of bone formation

As shown in Fig. 7e and f, the bone defects in the BM-based groups started to heal at 8 weeks post-surgery. Histomorphometric analysis of

the newly formed bone tissues indicated that the BV/TV indices of the BM/CP and BM/PLAT/CP groups were both 1.3-fold greater than that of the Ti group for the entire implantation period. No significant difference ( $p > 0.5$ ) was observed between the two BM-based groups. Moreover, compared with those in the Ti group, the BM/CP and BM/PLAT/CP groups exhibited significant increment in trabecular number (Tb.N) and trabecular thickness (Tb.Th), the values of which were 1.3 fold and 1.55 fold than Ti group respectively. and decreased trabecular spacing (Tb.Sp) at 16 week. There was no significant difference between the BM/CP and BM/PLAT/CP groups. The trabecular spacing (Tb.Sp) was decreased in BM/CP and BM/PLAT/CP groups at 16 week (Fig. 7g). Taken together, these findings suggested that the incorporation of Taxol into BM-based implants, which ensured controlled drug release, had negligible adverse influence on the bone remodeling process during femoral defect healing and thus results in outstanding bone-forming capability

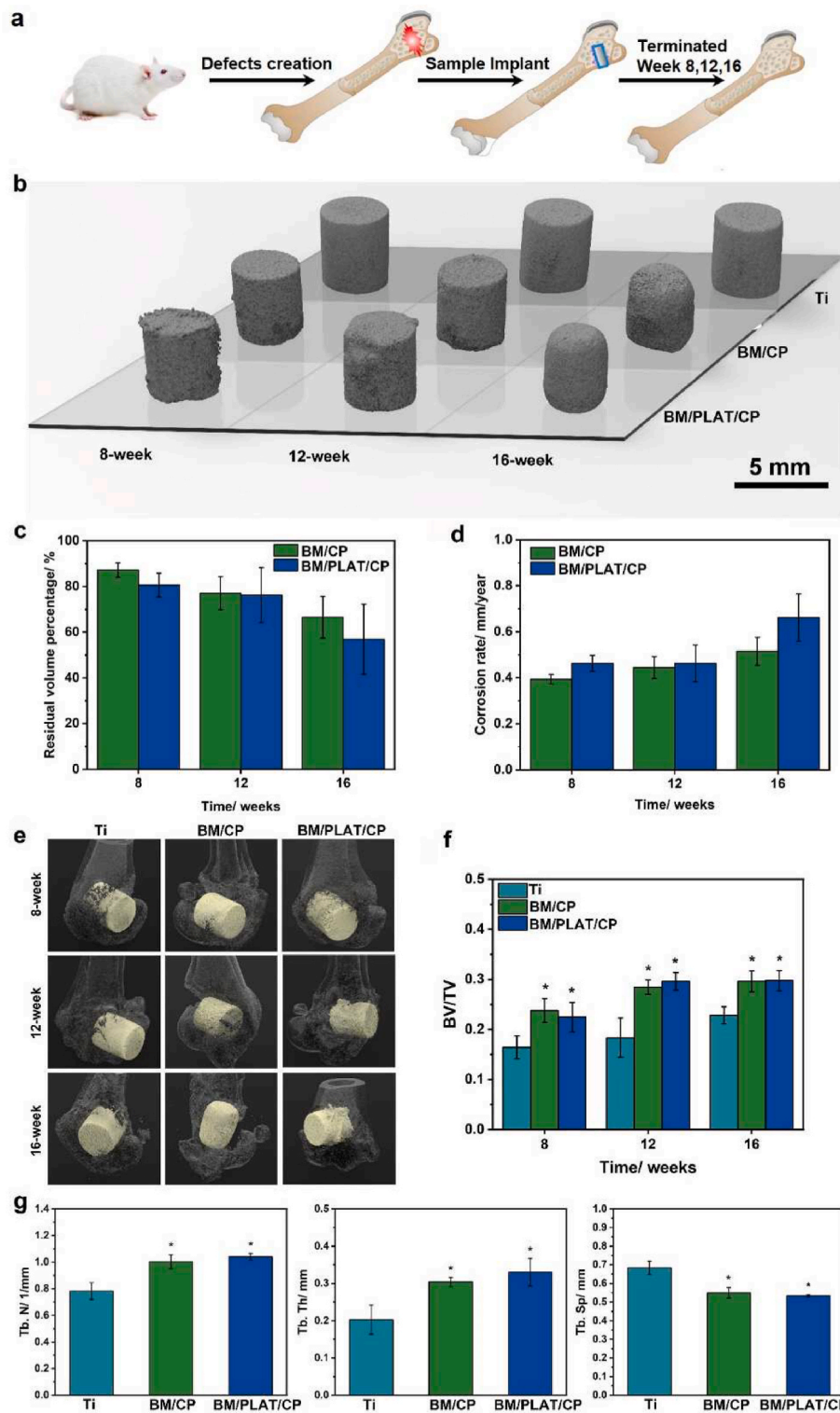


**Fig. 7.** Micro-CT images and histomorphometry analyses. a) Schematic illustration of femoral defect model establishment and therapy process of BM/PLAT/CP. b) 3D-reconstructed micro-CT images of Ti, BM/CP, and BM/PLAT/CP implants at different weeks post-surgery, respectively. c) The volume change and d) calculated corrosion rate of implants at different weeks post-surgery. e) Micro-CT images of different groups at week 8, 12, and 16 after implantation f) Bone volume fraction (BV/TV) of implants groups at different weeks post-surgery. g) Trabecular thickness (Tb. Th), trabecular spacing (Tb. Sp), and trabecular number (Tb. N) of different implant group at 16 weeks post-surgery. \**p* < 0.05.

with the Mg-based implants of controlled degradation.

### 2.5.3. Histological observation and analysis

Histological images acquired at 8, 12, and 16 weeks post-implantation of Ti, BM/CP, and BM/PLAT/CP are displayed in Fig. 8a

and b. The newly formed bone was microscopically observed in direct contact with the BM/CP and BM/PLAT/CP implants from week 8 onwards, and the bone trabeculae were arranged in well-organized order. In contrast, newly formed bone was indirectly connected in the Ti group. The bone-implant contact ratio results demonstrated that bone ingrowth

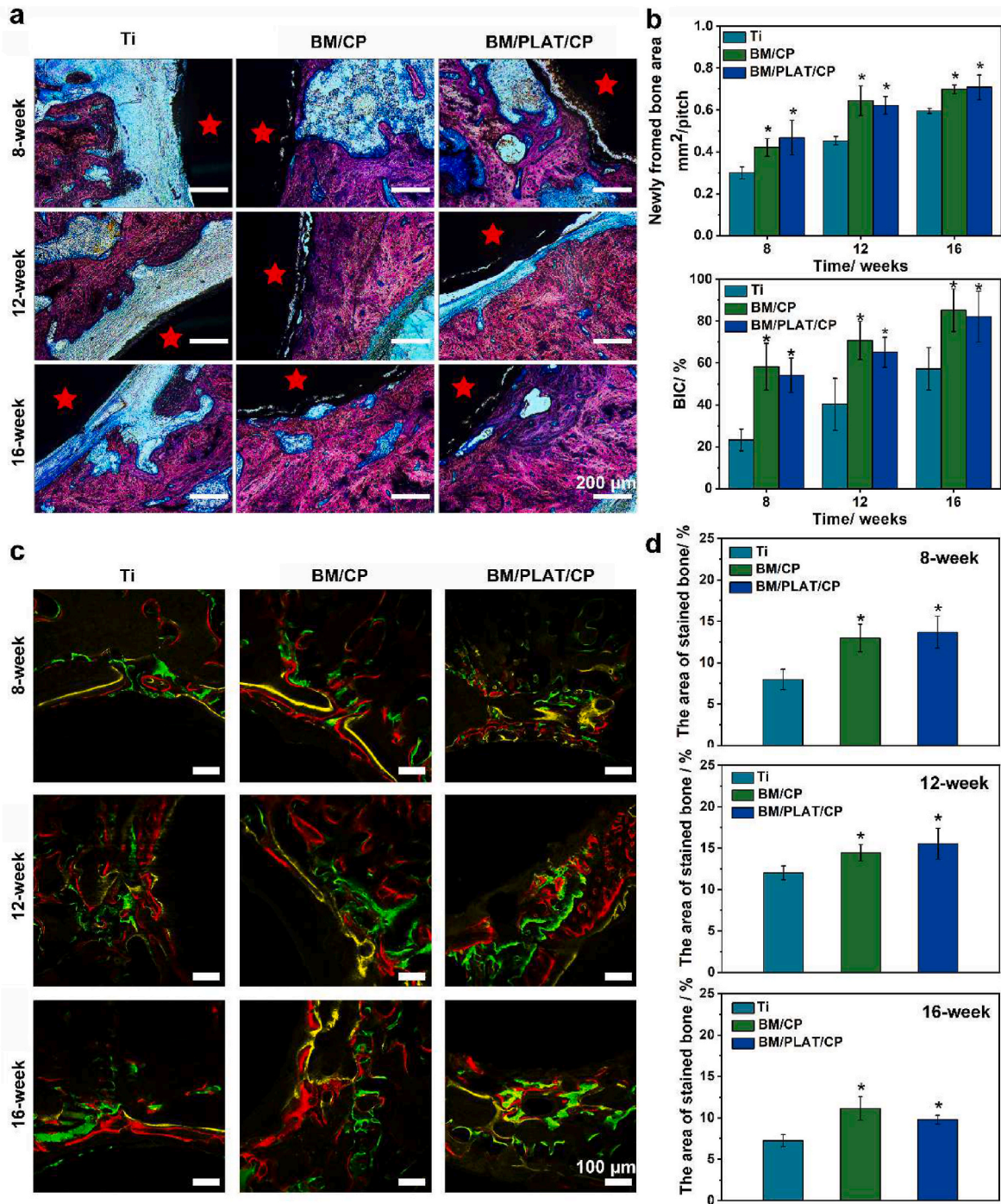


**Fig. 8.** *In vivo* analysis of the new bone formation of implants. a) Histologic overview of Ti, BM/CP, and BM/PLAT/CP implanted in femoral defects and b) quantification of the new bone area and BIC at different weeks post-surgery. Van Gieson’s picrofuchsin staining (scale bar = 200  $\mu$ m). The asterisk represents the implant. c, d) Sequential fluorescent labeling observation of Ti, BM/CP, and BM/PLAT/CP groups. The percentage of stained bone area is presented correspondingly. Scale bar = 100  $\mu$ m \**p* < 0.05.

was appreciably greater in the BM-based groups than in the Ti group in the first 8 weeks, during which virtually identical trends were maintained at 12 and 16 weeks post-surgery. The continuity and thickness of the trabeculae surrounding the BM-based implants continued to increase after 8 weeks. As shown in Fig. 8b, at 16 weeks post-surgery, remarkably more new bone was formed in the BM/CP and BM/PLAT/CP groups, which was approximately 1.3-fold greater than that in the Ti group.

New bone formation around Ti, BM/CP, and BM/PLAT/CP implants was recorded by using three fluorochromes. Bone formation at 16, 12, and 8 weeks post-surgery was analyzed via immune-fluorescent labeling

(Fig. 8c and d). The percentage of the stained bone area in the BM/CP and BM/PLAT/CP groups was significantly greater than that in the Ti group at 8 and 12 weeks. The osteoinductivity effect was most apparent in both BM-based groups, indicating that the controlled release of Mg biodegradation products was beneficial for inducing bone regeneration. The percentage of stained bone area decreased overall, signifying the occurrence of bone remodeling at 16 weeks post-surgery.

### 3. Discussion

In clinical practice, one of the critical challenges that persists lies in the regeneration of bone defects following surgery for bone tumors while simultaneously preventing the recurrence of bone cancer, and alleviating side effects of conventional chemotherapy. Hence, in our study, a bilayer PLA/CP-coated Mg-based implant was developed as a local drug delivery system to achieve sustainable and controllable release of chemotherapeutic Taxol for weeks. Additionally, the controlled degradation processes facilitated the successful regeneration of bone tissue. Mg alloy implants can promote osteogenic differentiation and improve femur fracture healing, suggesting the potential therapeutic effect of Mg in orthopedics [39]. Controlling the degradation of implants is crucial not only for preventing premature mechanical failure, but also for circumventing negative effects of excessive  $Mg^{2+}$  on osteogenesis due to undesirable immunomodulation in macrophages [40] thus ensuring appropriate bone regeneration and remodeling. Moreover, overfast, burst release of  $H_2$  gas, an anti-tumor agent provided with adequate, long-term application, could be also effectively harnessed. A bio-Mg alloy developed by our group was used as the substrate material [41], the mechanical strength (>200 MPa) and ductility (min. 10 %) of which meet the requirement of implantation. The Taxol-loaded PLA/CP-coated Mg-based implant significantly improved the corrosion resistance of the substrate, the degradation rate of which is 0.201 mm/year *in vitro*. The incorporation of Taxol barely affected the degradation profile of the PLA/CP-coated BM implants. Further micro-CT analysis of the *in vivo* data also confirmed that the BM/PLAT/CP implant maintained full structural integrity via surface degradation during the 4-month bone defect healing process. The calculated *in vivo* degradation rate of the BM/PLAT/CP implants was much higher than that measured *in vitro* (immersion in DMEM), and this difference may be due to the combined influence of proteins, cells and the *in vivo* dynamic body fluid environment, which would accelerate the degradation of Mg-based implants [42]. The *in vivo* degradation rates of BM/PLAT/CP implants was less than 0.5 mm/year and significantly lower than that of the previously reported naked Mg implants [43]. The BM/PLAT/CP implants exhibited a favorable controlled degradation profile with desirable uniform corrosion mode and no gas pockets observed post-surgery, which could adequately meet clinical requirements for orthopedic implants applications [44].

The treatment of bone tumors is a complex process which is regulated by various factors, including drug type and tumor microenvironment, etc. We demonstrated that the BM/PLAT/CP implant had a remarkable tumor inhibition effect compared with that of the control and BM/CP implant. Compared to systemic administration/injection of high-dose Taxol, the BM/PLAT150/CP implant had a significantly greater tumor inhibition rate even with a much lower Taxol loading, thereby revealing the distinct advantage of localized chemotherapy. In addition to local Taxol delivery, the degradation products of Mg-based composite implants could also inhibit tumor cells [45]. Studies have reported that alkaline environment can induce apoptosis and necrosis of tumor cells [46]. Meanwhile, gaseous  $H_2$  as a major degradation product of Mg can be also deployed as a therapeutic agent to restrain tumor growth [47]. Moreover, the abnormal cytoplasmic accumulation of free calcium ions ( $Ca^{2+}$ ), contributed to damage and even cell death in tumor cell types by causing mitochondrial dysfunction [48]. Notably, *in vitro* cellular results of MNNG cells treated with BM/PLAT/CP implants confirmed that PTX and  $H_2$  in combination with  $Ca^{2+}$  overloading-induced mitochondrial dysfunction cooperate with chemotherapeutic drug to achieve optimal triple inhibition effect of osteosarcoma cells by activating the Cyt-c pathway.

In our study, the cell viability results of MNNG cells and MC3T3-E1 cells confirmed that high-concentration extract of Mg strongly induced cytotoxicity for both tumor cells and osteoblastic cells by changing the TME, while low-concentration of which led to scarce tumor cells inhibition. Thus, it is vital to appropriately modulate Mg biodegradation to

balance antitumor activity and bone tissue biocompatibility and osteoinductivity. Through facily adjusting the preparation conditions, the thickness and morphology of the coating were optimized to modulate the release of Mg biodegradation products in a controlled, sustainable manner. The cell viability of MC3T3-E1 cells was obviously enhanced in BM/CP group. Interestingly, the cell viability of MNNG cells decreased markedly in BM/CP and BM/PLAT/CP group. Calcium ions is a key factor in multiple cellular processes, including proliferation, metabolism, and death [49], it may be also related to the  $Ca^{2+}$  ions level of cells (Fig. 5). Kajander et al. showed that Ca stimulated early pre-osteoblastic cells migration and motility to promote osteogenesis [50]. The CP coating was engineered to enhance corrosion resistance by blocking water diffusion and ion attack, while also promoting bioactivity [51]. During the initial 14 days of the immersion test, the release of  $Mg^{2+}$  was curtailed by the CP coating. Subsequently, the corrosion rate of the CP coating accelerated, surpassing that of BM/MgF<sub>2</sub>, as indicated by a significant surge in  $Mg^{2+}$  release. By quantifying the degradation product of BM/PLAT/CP implant, the results indicated  $Mg^{2+}$ ,  $Ca^{2+}$  and  $OH^-$  were released in a much slower and controlled manner, resulting in a near-physiological condition with adequate pH,  $Mg^{2+}$  and  $Ca^{2+}$  concentration, and osmolality for cell survival and proliferation due to the significant protection of PLAT/CP dual coating. The controlled release of  $Mg^{2+}$  and  $Ca^{2+}$  had a synergistic effect, which was more effective in promoting bone regeneration and repair than the use of either Mg or Ca ions alone. Considering these factors, PLAT/CP coating also provided a more favorable microenvironment for the survival, proliferation, and function of osteoblastic cells. Overall, the synergistic effect of  $H_2$ , calcium overload and Taxol as degradation of BM/PLAT/CP was demonstrated in tumor-associated bone defect therapy, in which the side effects of Taxol release on osteoblastic cells could be greatly mitigated, while the inhibition of tumor cells could be enhanced by appropriate administration of Mg biodegradation products. However, the *in vitro* cytotoxicity tests were detected without considering elimination of degradable products from implants via body circulation *in vivo*, which might lead to the difference between *in vitro* and *in vivo* [52]. According to the results *in vivo*, the elevated osteogenesis effect was apparent in BM/PLAT/CP group, as demonstrated in Figs. 7 and 8 (Micro-CT imaging, histomorphometry analyses and sequential fluorescent labeling observation), indicating that the controlled release of Mg biodegradation products was beneficial for inducing *in vivo* bone regeneration.

On the other hand, successful implantation for bone defect repair relies on crucial osteointegration between the surface of the implant and the remodeling bone [53]. In this work, the BM/PLAT/CP implant exhibited advantages in terms of osteointegration over the Ti implant for fixation of the femoral intercondylar defect. The bone volume surrounding the BM/PLAT/CP implant remained relatively greater than that surrounding the Ti implant at each time point. Histological examination also demonstrated mature bone tissue ingrowth around the BM/PLAT/CP implants. Recently substantial evidence has demonstrated good osteointegration and bone ingrowth around Bio-Mg alloy implants [54] or calcium phosphate biomaterials [55]. Thus, the enhanced osteogenic differentiation of MC3T3-E1 osteoblastic cells by the BM/PLAT/CP implant may be mostly correlated to the bioactivity of magnesium and calcium present in the substrate and the coating, which contributed to osteoconductivity and osteoinductivity, demonstrated with the significant enhancement of *in vivo* new bone formation. With these favorable features, the BM/PLAT/CP implant showed great potential as an innovative, superior modality in the combined treatment of tumor-induced bone defects, though systematic studies of large-scale animal assays and clinical trials in long term are required prior to its translation into clinical practice.

### 4. Conclusion

In this study, to treat tumor-associated bone defect, a bifunctional

Mg-based composite implant was designed and successfully fabricated by incorporating the chemotherapeutic drug Taxol into a PLA/brushite coating platform on a Mg alloy implant to combine the beneficial properties of magnesium and local chemotherapy. The enhanced efficacy of the Mg-based implant strategy was verified through its synergistic biological functions of antitumor activity and promoted osteogenesis both *in vitro* and *in vivo*. The excellent chemotherapeutic effect of this implant on killing bone tumor cells and restraining tumor growth *in vivo*, was associated with controlled release of degradation products of H<sub>2</sub> and Ca<sup>2+</sup>, along with the continuous modulation of TME, which effectively synergized the action of the local delivery of chemotherapeutic drug. Moreover, the well-orchestrated degradation of the implant also led to significant enhancement of osteoinductivity and boosted bone formation *in vivo*. Thus, by leveraging controlled degradation of the Mg-based implants, it not only assured appropriate degeneration of structural integrity throughout the bone healing process, but also contributed to the desirable bio-functions of promoted osteogenesis and tumor suppression, owing to the sustainable release of degradation products. Hence, our study demonstrated excellent potential of an innovative multifunctional Mg-based implant modality for application in tumor-associated bone defect.

## 5. Experimental section

### 5.1. Materials and sample preparation

The bio-Mg-based mixture, which consisted of Mg–Re alloy (abbreviated as BM), was used as the substrate and was prepared according to the previous methods [41]. Poly (D,L-lactic acid) (100,000 Mw) and Taxol were obtained from MedChemExpress LLC. (US). All the other chemicals and reagents used were of analytical grade. Briefly, 200 mg of PLA and Taxol (60 mM) were dissolved in 5 mL of ethyl acetate. The preparation was subsequently performed according to previous methods [56]. The PLA layer and calcium phosphate (CP) coating were prepared sequentially by dip-coating and chemical solution deposition methods, respectively, where simple UV activation treatment was applied to the PLA layer to enhance the heterogeneous nucleation of CP. Finally, a Taxol loading of  $2.10 \pm 0.10 \mu\text{g}/\text{mm}^2$  was achieved for each sample. The resultant BM sample was designated as BM/PLAT/CP, and the BM samples coated with calcium phosphate and PLA loaded with Taxol were denoted as BM/CP and BM/PLAT, respectively. BM disc specimens were subjected to *in vitro* studies, including extract preparation, immersion tests, and cellular response evaluations. BM disk specimens ( $\Phi 6 \text{ mm} \times 2 \text{ mm}$ ) were used for *in vivo* antitumor evaluation, and cylindrical specimens ( $\Phi 3.5 \text{ mm} \times 5 \text{ mm}$ ) were for *in vivo* degradation and osteogenesis evaluation.

### 5.2. Sample characterizations

The samples were embedded in poly (methyl methacrylate) to obtain cross-sections for analysis. The surface and cross-section of the samples were ground, starting from 300 to 7000 grits, using SiC paper. The samples were subsequently examined under a scanning electron microscope (SEM-EDS, JSM-7800 F Prime, Japan) to assess the coating thickness and structure integrity. BM/PLAT/CP was subjected to the “Tape Test” in accordance with the ASTM D3359-97 standard procedure. A 3 M scotch transparent tape (44 N/100 mm) was utilized to attach onto the cross-hatch pattern area on the test specimen followed by a quick removal of the tape. The interfacial adhesion level of the coating was assessed by comparing the ratio of the defected/detached region to the total area of the initial cross-hatch pattern. This resulted in a grading scale from 0 B (the least adhesion) to 5 B (the highest adhesion).

### 5.3. *In vitro* degradation of the implant

The samples were incubated in DMEM (Gibco, USA) at 37 °C and 5 %

CO<sub>2</sub> for 60 days. The concentration of Mg<sup>2+</sup> in the extract was determined using an inductively coupled plasma atomic emission spectrometer (icap6300, USA). Additionally, the pH was measured with a pH meter (FE20, Mettler Toledo, Switzerland), and the osmolality was assessed via an osmometer (Osmolality 3000, Gonotec, Germany). The *in vitro* biodegradation rate of Mg was meticulously calculated by analyzing the weight variances. Upon completion of the immersion test, the samples were extracted from the medium and examined using SEM–EDS.

### 5.4. *In vitro* drug release

The BM/PLAT/CP construct was carefully immersed in a solution of phosphate-buffered saline (PBS, pH = 7.4) with 1.0 % v/v of Tween 20 within a shaking incubator (120 rpm, 37 °C). At specific time intervals, 2 mL of the medium was meticulously extracted for analysis through a UV/Vis spectrophotometer (UH5300, Hitachi, Japan) at the characteristic wavelength of 228 nm, after which the medium was promptly replaced with an equal volume of fresh medium.

### 5.5. Cellular experiments

#### 5.5.1. Preparation of extracts

Aseptic samples were immersed in  $\alpha$ -MEM (Gibco, USA), enriched with 10 % FBS (Gibco, USA), and incubated for 3 days to procure the extracts. The ratio of sample area to medium volume adhered to the ISO 10993-5 standard and was set at 1.25 cm<sup>2</sup>/mL.

#### 5.5.2. Cell adhesion, viability and proliferation assays

MNNG or MC3T3-E1 cells ( $1 \times 10^4$  cells/well) were seeded in 24-well plates containing aseptic samples. The plates were incubated for 1, 3, or 5 days. Following the incubation period, the adherent cells were rinsed with PBS, subsequently stained with a Live/Dead staining kit (Thermo Fisher, USA) for 15 min and observed via fluorescence microscopy (IX71, Olympus, Japan). MNNG or MC3T3-E1 cells were seeded in a 96-well plate overnight and then incubated with sample extracts for 1, 3 or 5 days. The CCK8 assay (DOJINDO, Japan) was used to detect the viability and proliferation of MNNG cells.

#### 5.5.3. Alkaline phosphatase (ALP) expression

Adherent MC3T3-E1 cells were incubated with sample extracts supplemented with 100 nM of dexamethasone (Sigma, USA), 50  $\mu\text{M}$  ascorbic acid (Sigma, USA), or 10 mM  $\beta$ -glycerophosphate (Sigma, USA) for 7 or 14 days. The ALP activity was measured using pNPP as the substrate at 415 nm. The OD values were normalized to the total protein concentration (via a BCA Protein Assay Kit).

#### 5.5.4. Real-time PCR analysis

The mRNA expression levels of Alp, Opn, Col I, and Runx 2 were assessed, with GAPDH serving as the reference gene. In brief,  $1 \times 10^4$  MC3T3-E1 cells/well were cultured with the extract for 14 days. Total RNA was isolated from the MC3T3-E1 cells using TRIzol reagent (Ambion, Life Technologies, USA), and cDNA was synthesized using ReverTra Ace- $\alpha$  (TOYOBO, Japan). The resulting cDNA was subsequently amplified using SYBR Green Real-time PCR Master Mix (TOYOBO, Japan). RT–PCR analysis was conducted using a CFX96 Touch RT–PCR Detection System (Bio-Rad, USA) following the manufacturer’s protocol. The primer sequences for Alp, Opn, Col I, Runx 2, and GAPDH can be found in Table S1.

#### 5.5.5. Effect of magnesium degradation products on cells

Extracts of naked BM samples at different dilutions (100 %, 80 %, 50 %, and 20 % conc.) were prepared to estimate the effect of magnesium biodegradation products on cells. MC3T3-E1 or MNNG cells were seeded in 96-well plates at a density of  $2 \times 10^3$  cells/well. The procedure for determining cell viability was the same as that described in Section

## 5.5.2.

### 5.5.6. Measurement of $Ca^{2+}$ ion levels and mitochondrial dysfunction in osteosarcoma cells

MNNG cells were seeded at a density of  $1 \times 10^5$  cells/well in a 24-well Transwell plate and cultivated with complete  $\alpha$ -MEM (1 mL per well) in a cell incubator. After 12 h of cell attachment, the sterile samples were placed in the upper chamber of a 24-well plate. After 2 h, the mitochondrial membrane potential probe (DOJINDO, Japan) or Ca ion probe (Thermo Fisher, USA) was added, the mixture was incubated for 15 min and rinsed with  $\alpha$ -MEM 3 times. Subsequently, the cells were detected by fluorescence microscopy (IX71, Olympus, Japan). The mean values of fluorescence intensity were obtained by a microplate reader.

### 5.5.7. Western blot analysis

To analyze the underlying anti-tumor mechanisms, MNNG cells were incubated in 6-well plates at a density of  $2 \times 10^5$  cells per well for 12 h, and the sterile samples were placed in the upper chamber of a 6-well plate. After 24 h, respectively. The expression of Bcl-2 (ab182858, 1:2000) and Cyt-c (ab133504, 1:5000, Abcam, UK) was analyzed via WB (Image Tanon-5200 Multi).

### 5.5.8. Measurement of ROS level in MNNGs cells

MNNGs cells were seeded at a density of  $1 \times 10^5$  cells/well in 24-Transwell plate. After 12 h for cell attachment, the sterile samples were placed in the upper chamber of the 24-transwell plate. After incubation for 2 h and 24 h, respectively, the culture medium was replaced with  $\alpha$ -MEM containing 0.1 % DCFH-DA probe, incubated for 15 min, and observed with the fluorescence microscope (IX71, Olympus, Japan). The mean ROS values were obtained by ImageJ software based on the fluorescence intensities. The normalized ROS values were calculated as follows:

Normalized ROS value = Mean fluorescent intensity/Cell number

## 5.6. In vivo animal experiments

### 5.6.1. Animals

All animal experiments were performed according to the guidelines approved by the Animal Research Committee of the Sixth People's Hospital, Shanghai Jiao Tong University. SD rats (3 months old) and BALB/c nude mice (5 weeks old) (Shanghai Sippr-BK Laboratory Animal Co. Ltd., Shanghai, China) were used.

### 5.6.2. In vivo antitumor evaluation

BM disc samples from the MNNG osteosarcoma model were subjected to *in vivo* antitumor evaluation. A suspension containing  $1 \times 10^7$  of MNNG osteosarcoma cells was subcutaneously injected into BALB/c nude mice, which reached a volume of approximately 200 mm<sup>3</sup>. Sterile samples were implanted next to the tumor. The mice were divided into five groups (10 mice in each group): control (saline injection), Taxol injection (10 mg/kg, intraperitoneal injection), BM/CP implantation, BM implant loading ca. 45  $\mu$ g of Taxol (BM/PLAT45/CP), and BM implant loading ca. 150  $\mu$ g of Taxol (BM/PLAT150/CP). The tumor volume ( $V_{\text{Tumor}}$ ) at each time point was calculated according to the following formula:

$$V_{\text{Tumor}} = \text{Length}_{\text{Tumor}} \times \text{Width}_{\text{Tumor}}^2/2$$

$V_0$  refers to the initial tumor volume. The relative tumor size was calculated as  $V_{\text{Tumor}}/V_0$ . The nude mice were sacrificed 1 week post-surgery. The tumors were obtained, stained with hematoxylin & eosin (H&E) and finally examined to visualize the tumor tissue under an optical microscope.

### 5.6.3. In vivo osteogenesis

BM cylindrical samples were used for *in vivo* osteogenic evaluation.

Bone regeneration was estimated in SD rats by establishing a critical-sized femoral defect model. Sterile samples were implanted into the created bone defects ( $\Phi 3.5$  mm  $\times$  6 mm). The incisions were closed in layers. The polychrome sequential fluorescent labeling method was employed to assess new bone formation and mineralization. At 21, 14, and 7 days before the animals were sacrificed, fluorochromes were *i. p.* administered in a specific sequence of 20 mg/kg calcein, 30 mg/kg alizarin red S and 25 mg/kg tetracycline hydrochloride (Sigma–Aldrich, USA), respectively. As an accurate analyzing technique, micro-CT was performed to evaluate bone defect healing and *in vivo* degradation. 3D images were reconstructed based on 2D microtomography images using Amira (Visualization Science Group, USA).

SD rats were sacrificed at 8, 12, and 16 weeks post-surgery. After micro-CT analysis, femur specimens were dehydrated, embedded, cut into 150  $\mu$ m-thick sections and polished to obtain a final thickness of  $\sim$ 50  $\mu$ m. CLSM (Leica, TCS SP8 STED 3X, Germany) was used to observe the fluorescence. The sections were then counterstained with Van Gieson's picrofuchsin, and the mineralized bone tissue was examined under an optical microscope. The images were analyzed using ImageJ (version 6.0). The percentage of bone-implant contact ratio (BIC) was determined as follows:

BIC = bone contact length/implant length within one pitch  $\times$  100%

### 5.6.4. In vivo degradation

Micro-CT was conducted to detect the degradation of the BM-based samples in rats according to the volume loss. The residual volumes of the BM-based samples at 8, 12, and 16 weeks post-surgery were calculated via 3D remodeling through the use of a threshold of gray values.

## 5.7. Statistical analysis

All data were expressed as mean  $\pm$  standard deviation from at least three independent experiments. The results were analyzed via Student's t-test or ANOVA using SPSS software vc9 (IBM, USA).  $p < 0.05$  was considered to be statistically significant.

## Ethics approval and consent to participate

Animal experiments were approved by the Animal Care and Experimental Committee of the Sixth People's Hospital affiliated to School of Medicine, Shanghai Jiao Tong University (SYSK2021-0020).

## Declaration of competing interest

The authors declare no competing financial interest.

## CRediT authorship contribution statement

**Qingqing Guan:** Writing – review & editing, Writing – original draft, Visualization, Methodology, Investigation, Conceptualization. **Tu Hu:** Visualization, Methodology, Investigation. **Lei Zhang:** Writing – original draft, Visualization, Methodology, Investigation. **Mengjiao Yu:** Investigation. **Jialin Niu:** Methodology. **Zhiguang Ding:** Conceptualization. **Pei Yu:** Conceptualization. **Guangyin Yuan:** Supervision, Funding acquisition, Conceptualization. **Zhiquan An:** Writing – review & editing, Supervision, Funding acquisition, Conceptualization. **Jia Pei:** Writing – review & editing, Supervision, Funding acquisition, Conceptualization.

## Declaration of competing interest

The authors declare that they have no known competing financial interests or personal relationships that could have appeared to influence the work reported in this paper.

## Acknowledgements

This work was financially supported by the National Key Research & Development Program of China (2021YFE0204900), the National Natural Science Foundation of China (52222108), and Science and Technology Commission of Shanghai Municipality (22ZR1432000, 23JC1402400).

## Appendix A. Supplementary data

Supplementary data to this article can be found online at <https://doi.org/10.1016/j.bioactmat.2024.06.026>.

## References

- R.E. Coleman, P.I. Croucher, A.R. Padhani, P. Clézardin, E. Chow, M. Fallon, T. Guise, S. Colangeli, R. Capanna, L. Costa, *Nat. Rev. Dis. Prim.* 6 (2020) 83, <https://doi.org/10.1038/s41572-020-00216-3>.
- J. Gill, R. Gorlick, *Nat. Rev. Clin. Oncol.* 18 (2021) 609–624, <https://doi.org/10.1038/s41571-021-00519-8>.
- Y.X. Bian, X.J. Cai, Z.H. Lv, Y.M. Xu, H. Wang, C.L. Tan, R.Z. Liang, X.S. Weng, *Adv. Sci.* 10 (2023) 2301806, <https://doi.org/10.1002/adv.202301806>.
- Z.H. Jing, W.Q. Yuan, J.D. Wang, R.H. Ni, Y. Qin, Z.N. Mao, F. Wei, C.L. Song, Y. F. Zheng, H. Cai, Z.J. Liu, *Bioact. Mater.* 33 (2024) 223–241, <https://doi.org/10.1016/j.bioactmat.2023.11.001>.
- P.F. Sun, F. Qu, C. Zhang, P.F. Cheng, X.Y. Li, Q.M. Shen, D.F. Li, Q.L. Fan, *Adv. Sci.* 9 (2022) 2204718, <https://doi.org/10.1002/adv.202204718>.
- S. Zhang, Y. Yin, H. Xiong, *JAMA Oncol.* 10 (2024) 448–455, <https://doi.org/10.1001/jamaoncol.2023.6520>.
- J.F. Liao, R. Han, Y.Z. Wu, Z.Y. Qian, *Bone Res* 9 (2021) 18, <https://doi.org/10.1038/s41413-021-00139-z>.
- D.M. Gianfrante, L. Mirabello, S.A. Savage, *Nat. Rev. Endocrinol.* 13 (2017) 480–491, <https://doi.org/10.1038/nrendo.2017.16>.
- Z.F. Zhang, X. Liu, D.W. Chen, J.M. Yu, *Signal Transduct. Targeted Ther.* 7 (2022) 258, <https://doi.org/10.1038/s41392-022-01102-y>.
- J.F. Liao, K. Shi, Y.P. Jia, Y.T. Wu, *Bioact. Mater.* 6 (2021) 2221–2230, <https://doi.org/10.1016/j.bioactmat.2021.01.006>.
- R. Zhang, X. Song, C. Liang, X. Yi, G. Song, Y. Chao, Y. Yang, K. Yang, L. Feng, Z. Liu, *Biomaterials* 138 (2017) 13–21, <https://doi.org/10.1016/j.biomaterials.2017.05.025>.
- M.T. Manzari, Y. Shamay, H. Kiguchi, N. Rosen, M. Scaltriti, D.A. Heller, *Nat. Rev. Mater.* 6 (2021) 351–370, <https://doi.org/10.1038/s41578-020-00269-6>.
- P. Wei, J.S. Moosder, *Nat. Mater.* 19 (2020) 481–482, <https://doi.org/10.1038/s41578-020-0628-5>.
- M. Hao, H. Xia, J. Duan, H. Zhou, G. Zhang, D. Li, X. Chen, W. Wang, Y. Sang, S. Feng, H. Liu, *Adv. Funct. Mater.* 32 (2022) 2201013, <https://doi.org/10.1002/adfm.202201013>.
- Z. Wang, I.C.M. van der Geest, S.C.G. Leeuwenburgh, J.J.J.P. van den Beucken, *Mater. Today Bio* 23 (2023) 100889, <https://doi.org/10.1016/j.mtbio.2023.100889>.
- E. Roddy, M.R. DeBaun, A. Daoud-Gray, Y.P. Yang, M.J. Gardner, *Eur. J. Orthop. Surg. Traumatol.* 28 (2018) 351–362, <https://doi.org/10.1007/s00590-017-2063-0>.
- H.S. Ma, C. Jiang, D. Zhai, Y.X. Luo, Y. Chen, F. Lv, Z.F. Yi, Y. Deng, J.W. Wang, J. Chang, C.T. Wu, *Adv. Funct. Mater.* 26 (2016) 1197–1208, <https://doi.org/10.1002/adfm.201504142>.
- L. Zhang, G.Z. Jia, M. Tang, C.X. Chen, J.L. Niu, H. Huang, B. Kang, J. Pei, H. Zeng, G.Y. Yuan, *Mater. Sci. Eng., C* 111 (2020) 110779, <https://doi.org/10.1016/j.msec.2020.110779>.
- P.D. Tong, Y.L. Sheng, R.Q. Hou, M. Iqbal, L. Chen, J.G. Li, *Smart Mater Med* 3 (2022) 104–116, <https://doi.org/10.1016/j.smain.2021.12.007>.
- Z. Yuan, Z. Wan, C. Gao, Y. Wang, J. Huang, Q. Cai, *J. Contr. Release* 350 (2022) 360–376, <https://doi.org/10.1016/j.jconrel.2022.08.036>.
- W. Qiao, K. Wong, J. Shen, J. Wu, J.H. Li, Z.J. Lin, Z.T. Chen, J. Matinlinna, Y. F. Zheng, S.L. Wu, X.Y. Liu, K. Lai, Z.F. Chen, Y. Lam, K. Cheung, K. Yeung, *Nat. Commun.* 12 (2021) 2885, <https://doi.org/10.1038/s41467-021-23005-2>.
- C. Gao, S. Li, L. Liu, S. Bin, Y. Yang, S. Peng, C. Shuai, *J. Magnesium Alloys* 9 (2021) 305–316, <https://doi.org/10.1016/j.jma.2020.03.016>.
- J. Chen, P. Wu, Q. Wang, Y. Yang, S. Peng, Y. Zhou, C. Shuai, Y. Deng, *Met. Basel* 6 (2016) 259, <https://doi.org/10.3390/met6110259>.
- Z.S. Lin, Y.H. Wei, H.Z. Yang, *APL Bioeng.* 8 (2024) 021504, <https://doi.org/10.1063/5.0191800>.
- N. Yang, F. Gong, B. Liu, Y. Hao, Y. Chao, H. Lei, X.n Yang, Y. Gong, X. Wang, Z. Liu, L. Cheng, *Nat. Commun.* 13 (2022) 2336, <https://doi.org/10.1038/s41467-022-29938-6>.
- G. Qi, B. Wang, X. Song, H. Li 1, Y. Jin, *Natl. Sci. Rev.* 7 (2020) 660–670, <https://doi.org/10.1093/nsr/nwz1199>.
- M.A. Khalili, E. Tamjid, *Sci. Rep.* 11 (2021) 8645, <https://doi.org/10.1038/s41598-021-87783-x>.
- M.S. Song, R.C. Zeng, Y.F. Ding, R.W. Li, M. Easton, I. Cole, N. Birbilis, X.B. Chen, *J. Mater. Sci. Technol.* 35 (2019) 535–544, <https://doi.org/10.1016/j.jmst.2018.10.008>.
- P. Zheng, B.B. Ding, R. Shi, Z.Y. Jiang, W.G. Xu, G. Li, J.X. Ding, X.S. Chen, *Adv. Mater.* 33 (2021) 2007426, <https://doi.org/10.1002/adma.202007426>.
- P. Zheng, B.B. Ding, Z.Y. Jiang, W.G. Xu, G. Li, J.X. Ding, X.S. Chen, *Nano Lett.* 21 (2021) 2088–2093, <https://doi.org/10.1021/acs.nanolett.0c04778>.
- L. Zhang, J. Pei, H. Wang, Y. Shi, J. Niu, F. Yuan, H. Huang, H. Zhang, G. Yuan, *ACS Appl. Mater. Interfaces* 9 (2017) 9437–9448, <https://doi.org/10.1021/acsami.7b00209>.
- C. Zink, H. Hall, D.M. Brunette, N.D. Spencer, *Biomaterials* 33 (2012) 8055–8061, <https://doi.org/10.1016/j.biomaterials.2012.07.037>.
- T. Higuchi, *J. Pharm. Sci. USSR* 52 (1963) 1145–1149, <https://doi.org/10.1002/jps.2600521210>.
- X. Huang, C.S. Brazel, *J. Contr. Release* 73 (2001) 121–136, [https://doi.org/10.1016/S0168-3659\(01\)00248-6](https://doi.org/10.1016/S0168-3659(01)00248-6).
- C.H. Chang, J. Qiu, D. O'Sullivan, M.D. Buck, T. Noguchi, J.D. Curtis, Q. Chen, M. Gindin, M.M. Gubin, G.J. van der Windt, *Cell* 162 (2015) 1229–1241, <https://doi.org/10.1016/j.cell.2015.08.016>.
- Y. Wang, R. Narasimamurthy, M. Qu, N. Shi, H. Guo, Y. Xue, N. Barker, *Nat. Can. (Ott.)* 5 (2024) 546–556, <https://doi.org/10.1038/s43018-024-00759-4>.
- F. Gong, J.C. Xu, B. Liu, N.L. Yang, L. Cheng, P. Huang, C.J. Wang, Q. Chen, C.F. Ni, Z. Liu, *Chem* 8 (2022) 268–286, <https://doi.org/10.1016/j.chempr.2021.11.020>.
- Z.Y. Ma, J. Zhang, W.Y. Zhang, F.F. Mohamed, Y.F. Zhang, L. Ge, H.Y. Han, *iScience* 23 (2020) 101049, <https://doi.org/10.1016/j.isci.2020.101049>.
- Y. Zhang, J. Xu, Y.C. Ruan, M.K. Yu, M. O'Laughlin, H. Wise, D. Chen, L. Tian, D. Shi, J. Wang, S. Chen, J.Q. Peng, D.H.K. Chow, X. Xie, L. Zheng, L. Huang, S. Huang, K. Leung, N. Lu, L. Zhao, H. Li, D. Zhao, X. Guo, K. Chan, F. Witte, H. C. Chan, Y. Zheng, L. Qin, *Nat. Med.* 22 (2016) 1160–1169, <https://doi.org/10.1038/nm.4162>.
- C. Li, C. Guo, V. Fitzpatrick, A. Ibrahim, M. J. Zwierstra, P. Hanna, A. Lechtig, A. Nazarian, S. J. Lin, D. L. Kaplan, *5* (2020) 61–81, <https://doi.org/10.1038/s41578-019-0150-z>.
- X.B. Zhang, G.Y. Yuan, L. Mao, J.L. Niu, P.H. Fu, W.J. Ding, *J. Mech. Behav. Biomed. Mater.* 7 (2012) 77–86, <https://doi.org/10.1016/j.jmbbm.2011.05.026>.
- J. Zhang, N. Kong, Y. Shi, J. Niu, L. Mao, H. Li, M. Xiong, G. Yuan, *Corrosion Sci.* 85 (2014) 477–481, <https://doi.org/10.1016/j.corsci.2014.04.020>.
- T. Kraus, S.F. Fischerauer, A.C. Hanzl, P.J. Uggowitzer, J.F. Löffler, A.M. Weinberg, *Acta Biomater.* 8 (2012) 1230–1238, <https://doi.org/10.1016/j.actbio.2011.11.008>.
- V. Tsakiris, C. Tardei, F.M. Clicinschi, *J. Magnesium Alloys* 9 (2021) 1884–1905, <https://doi.org/10.1016/j.jma.2021.06.024>.
- Y. Chen, M. Xiao, H. Zhao, B. Yang, *J. Mater. Chem. B* 3 (2015) 849–858, <https://doi.org/10.1039/C4TB01421A>.
- P. Globig, R. Willumeit-Römer, F. Martini, E. Mazzoni, B.J.C. Luthringer-Feyerabend, *Bioact. Mater.* 16 (2022) 320–333, <https://doi.org/10.1016/j.bioactmat.2021.12.031>.
- R. Zan, H. Wang, W. Cai, J. Ni, B.J.C. Luthringer-Feyerabend, W. Wang, H. Peng, W. Ji, J. Yan, J. Xia, C. Y. Song, X. Zhang, *Bioact. Mater.* 26 (2021) 3596–3607, <https://doi.org/10.1016/j.bioactmat.2021.07.026>.
- C. Giorgi, S. Marchi, P. Pinton, *Nat. Rev. Mol. Cell Biol.* 19 (2018) 713–730, <https://doi.org/10.1038/s41580-018-0052-8>.
- C. Giorgi, S. Marchi, P. Pinton, *Nat. Rev. Mol. Cell Biol.* 19 (2018) 713–730, <https://doi.org/10.1038/s41580-018-0052-8>.
- K. Kajander, S.V. Sirkkiä, P.K. Vallittu, T.J. Heino, Jorma A. Määttä, *Sci. Rep.* 13 (2023) 20587, <https://doi.org/10.1038/s41598-023-47883-2>.
- J.L. Niu, G.Y. Yuan, Y. Liao, L. Mao, J. Zhang, Y.P. Wang, F. Huang, Y. Jiang, Y. H. He, W.J. Ding, *Mater. Sci. Eng. C* 33 (2013) 4833–4841, <https://doi.org/10.1016/j.msec.2013.08.008>.
- J. Wang, F. Witte, T. Xi, Y. Zheng, K. Yang, Y. Yang, D. Zhao, J. Meng, Y. Li, W. Li, K. Chan, L. Qin, *Acta Biomater.* 9 (2013) 8561–8573, <https://doi.org/10.1016/j.actbio.2015.04.011>.
- V. Goriainov, R. Cook, J.M. Latham, D.G. Dunlop, R.O.C. Oreffo, *Acta Biomater.* 10 (2014) 4043–4057, <https://doi.org/10.1016/j.actbio.2014.06.004>.
- N. Wang, S. Yang, H. Shi, Y. Song, H. Sun, Q. Wang, L. Tan, S. Guo, *J. Magnesium Alloys* 10 (2022) 3327–3353, <https://doi.org/10.1016/j.jma.2022.11.014>.
- R. Drevet, J. Fauré, H. Benhayoune, *Coatings* 13 (2023) 1091, <https://doi.org/10.3390/coatings13061091>.
- L. Mao, L. Shen, J. Chen, Y. Wu, M. Kwak, Y. Lu, Q. Xue, J. Pei, L. Zhang, G. Yuan, R. Fan, J. Ge, W. Ding, *ACS Appl. Mater. Interfaces* 7 (2015) 5320–5330, <https://doi.org/10.1021/am5086885>.